PHYSICAL REVIEW D **76,** 012008 (2007)

$e^+e^- \to K^+K^-\pi^+\pi^-$, $K^+K^-\pi^0\pi^0$ and $K^+K^-K^+K^-$ cross sections measured with initial-state radiation

B. Aubert, M. Bona, D. Boutigny, Y. Karyotakis, J. P. Lees, V. Poireau, X. Prudent, V. Tisserand, and A. Zghiche
Laboratoire de Physique des Particules, IN2P3/CNRS et Université de Savoie, F-74941 Annecy-Le-Vieux, France

J. Garra Tico and E. Grauges
Universitat de Barcelona, Facultat de Fisica, Departament ECM, E-08028 Barcelona, Spain

L. Lopez and A. Palano
Università di Bari, Dipartimento di Fisica and INFN, I-70126 Bari, Italy

G. Eigen, B. Stugu, and L. Sun
University of Bergen, Institute of Physics, N-5007 Bergen, Norway

G. S. Abrams, M. Battaglia, D. N. Brown, J. Button-Shafer, R. N. Cahn, Y. Groysman, R. G. Jacobsen, J. A. Kadyk, L. T. Kerth, Yu. G. Kolomensky, G. Kukartsev, D. Lopes Pegna, G. Lynch, L. M. Mir, T. J. Orimoto, M. T. Ronan,* K. Tackmann, and W. A. Wenzel
Lawrence Berkeley National Laboratory and University of California, Berkeley, California 94720, USA

P. del Amo Sanchez, C. M. Hawkes, and A. T. Watson
University of Birmingham, Birmingham, B15 2TT, United Kingdom

T. Held, H. Koch, B. Lewandowski, M. Pelizaeus, T. Schroeder, and M. Steinke
Ruhr Universität Bochum, Institut für Experimentalphysik1, D-44780 Bochum, Germany

D. Walker
University of Bristol, Bristol BS8 1TL, United Kingdom

D. J. Asgeirsson, T. Cuhadar-Donszelmann, B. G. Fulsom, C. Hearty, N. S. Knecht, T. S. Mattison, and J. A. McKenna
University of British Columbia, Vancouver, British Columbia, Canada V6T 1Z1

A. Khan, M. Saleem, and L. Teodorescu
Brunel University, Uxbridge, Middlesex UB8 3PH, United Kingdom

V. E. Blinov, A. D. Bukin, V. P. Druzhinin, V. B. Golubev, A. P. Onuchin, S. I. Serednyakov, Yu. I. Skovpen, E. P. Solodov, and K. Yu. Todyshev
Budker Institute of Nuclear Physics, Novosibirsk 630090, Russia

M. Bondioli, S. Curry, I. Eschrich, D. Kirkby, A. J. Lankford, P. Lund, M. Mandelkern, E. C. Martin, and D. P. Stoker
University of California at Irvine, Irvine, California 92697, USA

S. Abachi and C. Buchanan
University of California at Los Angeles, Los Angeles, California 90024, USA

S. D. Foulkes, J. W. Gary, F. Liu, O. Long, B. C. Shen, and L. Zhang
University of California at Riverside, Riverside, California 92521, USA

H. P. Paar, S. Rahatlou, and V. Sharma
University of California at San Diego, La Jolla, California 92093, USA

J. W. Berryhill, C. Campagnari, A. Cunha, B. Dahmes, T. M. Hong, D. Kovalskyi, and J. D. Richman
University of California at Santa Barbara, Santa Barbara, California 93106, USA

T. W. Beck, A. M. Eisner, C. J. Flacco, C. A. Heusch, J. Kroseberg, W. S. Lockman, T. Schalk, B. A. Schumm, A. Seiden, D. C. Williams, M. G. Wilson, and L. O. Winstrom
University of California at Santa Cruz, Institute for Particle Physics, Santa Cruz, California 95064, USA

E. Chen, C. H. Cheng, F. Fang, D. G. Hitlin, I. Narsky, T. Piatenko, and F. C. Porter
California Institute of Technology, Pasadena, California 91125, USA

G. Mancinelli, B. T. Meadows, K. Mishra, and M. D. Sokoloff
University of Cincinnati, Cincinnati, Ohio 45221, USA

F. Blanc, P. C. Bloom, S. Chen, W. T. Ford, J. F. Hirschauer, A. Kreisel, M. Nagel, U. Nauenberg, A. Olivas, J. G. Smith, K. A. Ulmer, S. R. Wagner, and J. Zhang
University of Colorado, Boulder, Colorado 80309, USA

A. M. Gabareen, A. Soffer, W. H. Toki, R. J. Wilson, F. Winklmeier, and Q. Zeng
Colorado State University, Fort Collins, Colorado 80523, USA

D. D. Altenburg, E. Feltresi, A. Hauke, H. Jasper, J. Merkel, A. Petzold, B. Spaan, and K. Wacker
Universität Dortmund, Institut für Physik, D-44221 Dortmund, Germany

T. Brandt, V. Klose, M. J. Kobel, H. M. Lacker, W. F. Mader, R. Nogowski, J. Schubert, K. R. Schubert, R. Schwierz, J. E. Sundermann, and A. Volk
Technische Universität Dresden, Institut für Kern-und Teilchenphysik, D-01062 Dresden, Germany

D. Bernard, G. R. Bonneaud, E. Latour, V. Lombardo, Ch. Thiebaux, and M. Verderi
Laboratoire Leprince-Ringuet, CNRS/IN2P3, Ecole Polytechnique, F-91128 Palaiseau, France

P. J. Clark, W. Gradl, F. Muheim, S. Playfer, A. I. Robertson, and Y. Xie
University of Edinburgh, Edinburgh EH9 3JZ, United Kingdom

M. Andreotti, D. Bettoni, C. Bozzi, R. Calabrese, A. Cecchi, G. Cibinetto, P. Franchini, E. Luppi, M. Negrini, A. Petrella, L. Piemontese, E. Prencipe, and V. Santoro
Università di Ferrara, Dipartimento di Fisica and INFN, I-44100 Ferrara, Italy

F. Anulli, R. Baldini-Ferroli, A. Calcaterra, R. de Sangro, G. Finocchiaro, S. Pacetti, P. Patteri, I. M. Peruzzi,[†] M. Piccolo, M. Rama, and A. Zallo
Laboratori Nazionali di Frascati dell'INFN, I-00044 Frascati, Italy

A. Buzzo, R. Contri, M. Lo Vetere, M. M. Macri, M. R. Monge, S. Passaggio, C. Patrignani, E. Robutti, A. Santroni, and S. Tosi
Università di Genova, Dipartimento di Fisica and INFN, I-16146 Genova, Italy

K. S. Chaisanguanthum, M. Morii, and J. Wu
Harvard University, Cambridge, Massachusetts 02138, USA

R. S. Dubitzky, J. Marks, S. Schenk, and U. Uwer
Universität Heidelberg, Physikalisches Institut, Philosophenweg 12, D-69120 Heidelberg, Germany

D. J. Bard, P. D. Dauncey, R. L. Flack, J. A. Nash, M. B. Nikolich, and W. Panduro Vazquez
Imperial College London, London, SW7 2AZ, United Kingdom

P. K. Behera, X. Chai, M. J. Charles, U. Mallik, N. T. Meyer, and V. Ziegler
University of Iowa, Iowa City, Iowa 52242, USA

J. Cochran, H. B. Crawley, L. Dong, V. Eyges, W. T. Meyer, S. Prell, E. I. Rosenberg, and A. E. Rubin
Iowa State University, Ames, Iowa 50011-3160, USA

A. V. Gritsan and C. K. Lae
Johns Hopkins University, Baltimore, Maryland 21218, USA

A. G. Denig, M. Fritsch, and G. Schott
Universität Karlsruhe, Institut für Experimentelle Kernphysik, D-76021 Karlsruhe, Germany

N. Arnaud, J. Béquilleux, M. Davier, G. Grosdidier, A. Höcker, V. Lepeltier, F. Le Diberder, A. M. Lutz, S. Pruvot, S. Rodier, P. Roudeau, M. H. Schune, J. Serrano, V. Sordini, A. Stocchi, W. F. Wang, and G. Wormser
Laboratoire de l'Accélérateur Linéaire, IN2P3/CNRS et Université Paris-Sud 11, Centre Scientifique d'Orsay, B.P. 34, F-91898 Orsay Cedex, France

D. J. Lange and D. M. Wright
Lawrence Livermore National Laboratory, Livermore, California 94550, USA

C. A. Chavez, I. J. Forster, J. R. Fry, E. Gabathuler, R. Gamet, D. E. Hutchcroft, D. J. Payne, K. C. Schofield, and C. Touramanis
University of Liverpool, Liverpool L69 7ZE, United Kingdom

A. J. Bevan, K. A. George, F. Di Lodovico, W. Menges, and R. Sacco
Queen Mary, University of London, E1 4NS, United Kingdom

G. Cowan, H. U. Flaecher, D. A. Hopkins, P. S. Jackson, T. R. McMahon, F. Salvatore, and A. C. Wren
University of London, Royal Holloway and Bedford New College, Egham, Surrey TW20 0EX, United Kingdom

D. N. Brown and C. L. Davis
University of Louisville, Louisville, Kentucky 40292, USA

J. Allison, N. R. Barlow, R. J. Barlow, Y. M. Chia, C. L. Edgar, G. D. Lafferty, T. J. West, and J. I. Yi
University of Manchester, Manchester M13 9PL, United Kingdom

J. Anderson, C. Chen, A. Jawahery, D. A. Roberts, G. Simi, and J. M. Tuggle
University of Maryland, College Park, Maryland 20742, USA

G. Blaylock, C. Dallapiccola, S. S. Hertzbach, X. Li, T. B. Moore, E. Salvati, and S. Saremi
University of Massachusetts, Amherst, Massachusetts 01003, USA

R. Cowan, P. H. Fisher, G. Sciolla, S. J. Sekula, M. Spitznagel, F. Taylor, and R. K. Yamamoto
Massachusetts Institute of Technology, Laboratory for Nuclear Science, Cambridge, Massachusetts 02139, USA

S. E. Mclachlin, P. M. Patel, and S. H. Robertson
McGill University, Montréal, Québec, Canada H3A 2T8

A. Lazzaro and F. Palombo
Università di Milano, Dipartimento di Fisica and INFN, I-20133 Milano, Italy

J. M. Bauer, L. Cremaldi, V. Eschenburg, R. Godang, R. Kroeger, D. A. Sanders, D. J. Summers, and H. W. Zhao
University of Mississippi, University, Mississippi 38677, USA

S. Brunet, D. Côté, M. Simard, P. Taras, and F. B. Viaud
Université de Montréal, Physique des Particules, Montréal, Québec, Canada H3C 3J7

H. Nicholson
Mount Holyoke College, South Hadley, Massachusetts 01075, USA

G. De Nardo, F. Fabozzi,[‡] L. Lista, D. Monorchio, and C. Sciacca
Università di Napoli Federico II, Dipartimento diScienze Fisiche and INFN, I-80126, Napoli, Italy

M. A. Baak, G. Raven, and H. L. Snoek
NIKHEF, National Institute for Nuclear Physics and High Energy Physics, NL-1009 DB Amsterdam, The Netherlands

C. P. Jessop and J. M. LoSecco
University of Notre Dame, Notre Dame, Indiana 46556, USA

G. Benelli, L. A. Corwin, K. K. Gan, K. Honscheid, D. Hufnagel, H. Kagan, R. Kass, J. P. Morris, A. M. Rahimi, J. J. Regensburger, R. Ter-Antonyan, and Q. K. Wong
Ohio State University, Columbus, Ohio 43210, USA

N. L. Blount, J. Brau, R. Frey, O. Igonkina, J. A. Kolb, M. Lu, R. Rahmat, N. B. Sinev, D. Strom, J. Strube, and E. Torrence
University of Oregon, Eugene, Oregon 97403, USA

N. Gagliardi, A. Gaz, M. Margoni, M. Morandin, A. Pompili, M. Posocco, M. Rotondo, F. Simonetto, R. Stroili, and C. Voci
Università di Padova, Dipartimento di Fisica and INFN, I-35131 Padova, Italy

E. Ben-Haim, H. Briand, J. Chauveau, P. David, L. Del Buono, Ch. de la Vaissière, O. Hamon, Ph. Leruste, J. Malclès, J. Ocariz, and A. Perez
Laboratoire de Physique Nucléaire et de Hautes Energies, IN2P3/CNRS, Université Pierre et Marie Curie-Paris6, Université Denis Diderot-Paris7, F-75252 Paris, France

L. Gladney
University of Pennsylvania, Philadelphia, Pennsylvania 19104, USA

M. Biasini, R. Covarelli, and E. Manoni
Università di Perugia, Dipartimento di Fisica and INFN, I-06100 Perugia, Italy

C. Angelini, G. Batignani, S. Bettarini, M. Carpinelli, R. Cenci, F. Forti, M. A. Giorgi, A. Lusiani, G. Marchiori, M. A. Mazur, M. Morganti, N. Neri, E. Paoloni, G. Rizzo, and J. J. Walsh
Università di Pisa, Dipartimento di Fisica, Scuola Normale Superiore and INFN, I-56127 Pisa, Italy

M. Haire
Prairie View A&M University, Prairie View, Texas 77446, USA

J. Biesiada, P. Elmer, Y. P. Lau, C. Lu, J. Olsen, A. J. S. Smith, and A. V. Telnov
Princeton University, Princeton, New Jersey 08544, USA

E. Baracchini, F. Bellini, G. Cavoto, A. D'Orazio, D. del Re, E. Di Marco, R. Faccini, F. Ferrarotto, F. Ferroni, M. Gaspero, P. D. Jackson, L. Li Gioi, M. A. Mazzoni, S. Morganti, G. Piredda, F. Polci, F. Renga, and C. Voena
Università di Roma La Sapienza, Dipartimento di Fisica and INFN, I-00185 Roma, Italy

M. Ebert, H. Schröder, and R. Waldi
Universität Rostock, D-18051 Rostock, Germany

T. Adye, G. Castelli, B. Franek, E. O. Olaiya, S. Ricciardi, W. Roethel, and F. F. Wilson
Rutherford Appleton Laboratory, Chilton, Didcot, Oxon, OX11 0QX, United Kingdom

R. Aleksan, S. Emery, M. Escalier, A. Gaidot, S. F. Ganzhur, G. Hamel de Monchenault, W. Kozanecki, M. Legendre, G. Vasseur, Ch. Yèche, and M. Zito
DSM/Dapnia, CEA/Saclay, F-91191 Gif-sur-Yvette, France

X. R. Chen, H. Liu, W. Park, M. V. Purohit, and J. R. Wilson
University of South Carolina, Columbia, South Carolina 29208, USA

M. T. Allen, D. Aston, R. Bartoldus, P. Bechtle, N. Berger, R. Claus, J. P. Coleman, M. R. Convery, J. C. Dingfelder, J. Dorfan, G. P. Dubois-Felsmann, D. Dujmic, W. Dunwoodie, R. C. Field, T. Glanzman, S. J. Gowdy, M. T. Graham, P. Grenier, C. Hast, T. Hryn'ova, W. R. Innes, J. Kaminski, M. H. Kelsey, H. Kim, P. Kim, M. L. Kocian, D. W. G. S. Leith, S. Li, S. Luitz, V. Luth, H. L. Lynch, D. B. MacFarlane, H. Marsiske, R. Messner, D. R. Muller, C. P. O'Grady, I. Ofte,

A. Perazzo, M. Perl, T. Pulliam, B. N. Ratcliff, A. Roodman, A. A. Salnikov, R. H. Schindler, J. Schwiening, A. Snyder, J. Stelzer, D. Su, M. K. Sullivan, K. Suzuki, S. K. Swain, J. M. Thompson, J. Va'vra, N. van Bakel, A. P. Wagner, M. Weaver, W. J. Wisniewski, M. Wittgen, D. H. Wright, A. K. Yarritu, K. Yi, and C. C. Young
Stanford Linear Accelerator Center, Stanford, California 94309, USA

P. R. Burchat, A. J. Edwards, S. A. Majewski, B. A. Petersen, and L. Wilden
Stanford University, Stanford, California 94305-4060, USA

S. Ahmed, M. S. Alam, R. Bula, J. A. Ernst, V. Jain, B. Pan, M. A. Saeed, F. R. Wappler, and S. B. Zain
State University of New York, Albany, New York 12222, USA

W. Bugg, M. Krishnamurthy, and S. M. Spanier
University of Tennessee, Knoxville, Tennessee 37996, USA

R. Eckmann, J. L. Ritchie, A. M. Ruland, C. J. Schilling, and R. F. Schwitters
University of Texas at Austin, Austin, Texas 78712, USA

J. M. Izen, X. C. Lou, and S. Ye
University of Texas at Dallas, Richardson, Texas 75083, USA

F. Bianchi, F. Gallo, D. Gamba, and M. Pelliccioni
Università di Torino, Dipartimento di Fisica Sperimentale and INFN, I-10125 Torino, Italy

M. Bomben, L. Bosisio, C. Cartaro, F. Cossutti, G. Della Ricca, L. Lanceri, and L. Vitale
Università di Trieste, Dipartimento di Fisica and INFN, I-34127 Trieste, Italy

V. Azzolini, N. Lopez-March, F. Martinez-Vidal, D. A. Milanes, and A. Oyanguren
IFIC, Universitat de Valencia-CSIC, E-46071 Valencia, Spain

J. Albert, Sw. Banerjee, B. Bhuyan, K. Hamano, R. Kowalewski, I. M. Nugent, J. M. Roney, and R. J. Sobie
University of Victoria, Victoria, British Columbia, Canada V8W 3P6

J. J. Back, P. F. Harrison, T. E. Latham, G. B. Mohanty, and M. Pappagallo[§]
Department of Physics, University of Warwick, Coventry CV47AL, United Kingdom

H. R. Band, X. Chen, S. Dasu, K. T. Flood, J. J. Hollar, P. E. Kutter, Y. Pan, M. Pierini, R. Prepost, S. L. Wu, and Z. Yu
University of Wisconsin, Madison, Wisconsin 53706, USA

H. Neal
Yale University, New Haven, Connecticut 06511, USA
(Received 1 May 2007; published 31 July 2007)

We study the processes $e^+e^- \to K^+K^-\pi^+\pi^-\gamma$, $K^+K^-\pi^0\pi^0\gamma$ and $K^+K^-K^+K^-\gamma$, where the photon is radiated from the initial state. About 34 600, 4400 and 2300 fully reconstructed events, respectively, are selected from 232 fb^{-1} of *BABAR* data. The invariant mass of the hadronic final state defines the effective e^+e^- center-of-mass energy, so that the $K^+K^-\pi^+\pi^-\gamma$ data can be compared with direct measurements of the $e^+e^- \to K^+K^-\pi^+\pi^-$ reaction; no direct measurements exist for the $e^+e^- \to K^+K^-\pi^0\pi^0$ or $e^+e^- \to K^+K^-K^+K^-$ reactions. Studying the structure of these events, we find contributions from a number of intermediate states, and we extract their cross sections where possible. In particular, we isolate the contribution from $e^+e^- \to \phi(1020)f_0(980)$ and study its structure near threshold. In the charmonium region, we observe the J/ψ in all three final states and several intermediate states, as well as the $\psi(2S)$ in some modes, and measure the corresponding branching fractions. We see no signal for the $Y(4260)$ and obtain an upper limit of $\mathcal{B}_{Y(4260)\to\phi\pi^+\pi^-} \cdot \Gamma^Y_{ee} < 0.4$ eV at 90% C.L.

[*] Deceased.
[†] Also with Università di Perugia, Dipartimento di Fisica, Perugia, Italy.
[‡] Also with Università della Basilicata, Potenza, Italy.
[§] Also with IPPP, Physics Department, Durham University, Durham DH1 3LE, United Kingdom.

DOI: 10.1103/PhysRevD.76.012008 PACS numbers: 13.66.Bc, 13.25.Gv, 13.25.Jx, 14.40.Cs

I. INTRODUCTION

Electron-positron annihilation at fixed center-of-mass (c.m.) energies has long been a mainstay of research in elementary particle physics. The idea of utilizing initial-state radiation (ISR) to explore e^+e^- reactions below the nominal c.m. energies was outlined in Ref. [1], and discussed in the context of high-luminosity ϕ and B factories in Refs. [2–4]. At high energies, e^+e^- annihilation is dominated by quark-level processes producing two or more hadronic jets. However, low-multiplicity exclusive processes dominate at energies below about 2 GeV, and the region near charm threshold, 3.0–4.5 GeV, features a number of resonances [5]. These allow us to probe a wealth of physics parameters, including cross sections, spectroscopy and form factors.

Of particular current interest are the recently observed states in the charmonium region, such as the $Y(4260)$ [6], and a possible discrepancy between the measured value of the anomalous magnetic moment of the muon, $g_\mu - 2$, and that predicted by the standard model [7]. Charmonium and other states with $J^{PC} = 1^{--}$ can be observed as resonances in the cross section, and intermediate states may be present in the hadronic system. Measurements of the decay modes and their branching fractions are important in understanding the nature of these states. For example, the glueball model [8] predicts a large branching fraction for $Y(4260)$ into $\phi\pi\pi$. The prediction for $g_\mu - 2$ is based on hadronic-loop corrections measured from low-energy $e^+e^- \to$ hadrons data, and these dominate the uncertainty on the prediction. Improving this prediction requires not only more precise measurements, but also measurements over the entire energy range and inclusion of all the important subprocesses in order to understand possible acceptance effects. ISR events at B factories provide independent and contiguous measurements of hadronic cross sections from the production threshold to about 5 GeV.

The cross section for the radiation of a photon of energy E_γ followed by the production of a particular hadronic final state f is related to the corresponding direct $e^+e^- \to f$ cross section $\sigma_f(s)$ by

$$\frac{d\sigma_{\gamma f}(s,x)}{dx} = W(s,x)\cdot\sigma_f(s(1-x)), \qquad (1)$$

where $\sqrt{s}$ is the initial e^+e^- c.m. energy, $x = 2E_\gamma/\sqrt{s}$ is the fractional energy of the ISR photon and $E_{\rm c.m.} \equiv \sqrt{s(1-x)}$ is the effective c.m. energy at which the final state f is produced. The probability density function $W(s,x)$ for ISR photon emission has been calculated with better than 1% precision (see e.g. Ref. [4]). It falls rapidly as E_γ increases from zero, but has a long tail, which combines with the increasing $\sigma_f(s(1-x))$ to produce a sizable cross section at very low $E_{\rm c.m.}$. The angular distribution of the ISR photon peaks along the beam directions, but 10%–15% [4] of the photons are within a typical detector acceptance.

Experimentally, the measured invariant mass of the hadronic final state defines $E_{\rm c.m.}$. An important feature of ISR data is that a wide range of energies is scanned simultaneously in one experiment, so that no structure is missed and the relative normalization uncertainties in data from different experiments or accelerator parameters are avoided. Furthermore, for large values of x the hadronic system is collimated, reducing acceptance issues and allowing measurements at energies down to production threshold. The mass resolution is not as good as a typical beam energy spread used in direct measurements, but the resolution and absolute energy scale can be monitored by the width and mass of well-known resonances, such as the J/ψ produced in the reaction $e^+e^- \to J/\psi\gamma$. Backgrounds from $e^+e^- \to$ hadrons events at the nominal $\sqrt{s}$ and from other ISR processes can be suppressed by a combination of particle identification and kinematic fitting techniques. Studies of $e^+e^- \to \mu^+\mu^-\gamma$ and several multihadron ISR processes using *BABAR* data have been reported [9–12], demonstrating the viability of such measurements.

The $K^+K^-\pi^+\pi^-$ final state has been measured directly by the DM1 collaboration [13] for $\sqrt{s} < 2.2$ GeV, and we have previously published ISR measurements of the $K^+K^-\pi^+\pi^-$ and $K^+K^-K^+K^-$ final states [11] for $E_{\rm c.m.} < 4.5$ GeV. We recently reported [14] an updated measurement of the $K^+K^-\pi^+\pi^-$ final state with a larger data sample, along with the first measurement of the $K^+K^-\pi^0\pi^0$ final state, in which we observed a structure near threshold in the ϕf_0 intermediate state. In this paper we present a more detailed study of these two final states along with an updated measurement of the $K^+K^-K^+K^-$ final state. In all cases we require detection of the ISR photon and perform a set of kinematic fits. We are able to suppress backgrounds sufficiently to study these final states from their respective production thresholds up to 5 GeV. In addition to measuring the overall cross sections, we study the internal structure of the events and measure cross sections for a number of intermediate states. We study the charmonium region, measure several J/ψ and $\psi(2S)$ branching fractions, and set limits on other states.

II. THE *BABAR* DETECTOR AND DATA SET

The data used in this analysis were collected with the *BABAR* detector at the PEP-II asymmetric energy e^+e^- storage rings. The total integrated luminosity used is 232 fb^{-1}, which includes 211 fb^{-1} collected at the $Y(4S)$ peak, $\sqrt{s} = 10.58$ GeV, and 21 fb^{-1} collected below the resonance, at $\sqrt{s} = 10.54$ GeV.

The *BABAR* detector is described elsewhere [15]. Here we use charged particles reconstructed in the tracking system, which comprises the five-layer silicon vertex

tracker (SVT) and the 40-layer drift chamber (DCH) in a 1.5 T axial magnetic field. Separation of charged pions, kaons and protons uses a combination of Cherenkov angles measured in the detector of internally reflected Cherenkov light (DIRC) and specific ionization measured in the SVT and DCH. For the present study we use a kaon identification algorithm that provides 90%–95% efficiency, depending on momentum, and pion and proton rejection factors in the 20–100 range. Photon and electron energies are measured in the CsI(Tl) electromagnetic calorimeter (EMC). We use muon identification provided by the instrumented flux return (IFR) to select the $\mu^+\mu^-\gamma$ final state.

To study the detector acceptance and efficiency, we use a simulation package developed for radiative processes. The simulation of hadronic final states, including $K^+K^-\pi^+\pi^-\gamma$, $K^+K^-\pi^0\pi^0\gamma$ and $K^+K^-K^+K^-\gamma$, is based on the approach suggested by Czyż and Kühn [16]. Multiple soft-photon emission from the initial-state charged particles is implemented with a structure-function technique [17,18], and photon radiation from the final-state particles is simulated by the PHOTOS package [19]. The accuracy of the radiative corrections is about 1%.

We simulate the $K^+K^-\pi\pi$ final states both according to phase space and with models that include the $\phi(1020) \to K^+K^-$ and/or $f_0(980) \to \pi\pi$ channels, and the $K^+K^-K^+K^-$ final state both according to phase space and including the $\phi \to K^+K^-$ channel. The generated events go through a detailed detector simulation [20], and we reconstruct them with the same software chain as the experimental data. Variations in detector and background conditions are taken into account.

We also generate a large number of background processes, including the ISR channels $e^+e^- \to \pi^+\pi^-\pi^+\pi^-\gamma$ and $\pi^+\pi^-\pi^0\pi^0\gamma$, which can contribute due to particle misidentification, and $\phi\eta\gamma$, $\phi\pi^0\gamma$, $\pi^+\pi^-\pi^0\gamma$, which have larger cross sections and can contribute via missing or spurious tracks or photons. In addition, we study the non-ISR backgrounds $e^+e^- \to q\bar{q}$ ($q = u, d, s, c$) generated by JETSET [21] and $e^+e^- \to \tau^+\tau^-$ by KORALB [22]. The contribution from the $\Upsilon(4S)$ decays is found to be negligible. The cross sections for these processes are known with about 10% accuracy or better, which is sufficient for these measurements.

III. EVENT SELECTION AND KINEMATIC FIT

In the initial selection of candidate events, we consider photon candidates in the EMC with energy above 0.03 GeV and charged tracks reconstructed in the DCH or SVT or both that extrapolate within 0.25 cm of the beam axis in the transverse plane and within 3 cm of the nominal collision point along the axis. These criteria are looser than in our previous analysis [11], and have been chosen to maximize efficiency. We require a high-energy photon in the event with an energy in the initial e^+e^- c.m. frame of $E_\gamma > 3$ GeV, and either exactly four charged tracks with zero net charge and total momentum roughly opposite to the photon direction, or exactly two oppositely charged tracks that combine with a set of other photons to roughly balance the highest-energy photon momentum. We fit a vertex to the set of charged tracks and use it as the point of origin to calculate the photon direction. Most events contain additional soft photons due to machine background or interactions in the detector material.

We subject each of these candidate events to a set of constrained kinematic fits, and use the fit results, along with charged-particle identification, both to select the final states of interest and to measure backgrounds from other processes. We assume the photon with the highest E_γ in the c.m. frame is the ISR photon, and the kinematic fits use its direction along with the four-momenta and covariance matrices of the initial e^+e^- and the set of selected tracks and photons. Because of excellent resolution for the momenta in the DCH and good angular resolution for the photons in the EMC, the ISR photon energy is determined with better resolution through four-momentum conservation than through measurement in the EMC. Therefore we do not use its measured energy in the fits, eliminating the systematic uncertainty due to the EMC calibration for high-energy photons. The fitted three-momenta for each charged track and photon are used in further kinematical calculations.

For the four-track candidates, the fits have three constraints (3C). We first fit to the $\pi^+\pi^-\pi^+\pi^-$ hypothesis, obtaining a $\chi^2_{4\pi}$. If the four tracks include one identified K^+ and one K^-, we fit to the $K^+K^-\pi^+\pi^-$ hypothesis and retain the event as a $K^+K^-\pi^+\pi^-$ candidate. For events with one identified kaon, we perform fits with each of the two oppositely charged tracks given the kaon hypothesis, and the combination with the lower $\chi^2_{KK\pi^+\pi^-}$ is retained if it is lower than $\chi^2_{4\pi}$. If the event contains three or four identified $K^\pm$, we fit to the $K^+K^-K^+K^-$ hypothesis and retain the event as a $K^+K^-K^+K^-$ candidate.

For the events with two charged tracks and five or more photon candidates, we require both tracks to be identified as kaons to suppress background from ISR $\pi^+\pi^-\pi^0\pi^0$ and $K^\pm K^0_S\pi^\mp$ events. We then pair all non-ISR photon candidates and consider combinations with invariant mass within ± 30 MeV/c^2 of the π^0 mass as π^0 candidates. We perform a six-constraint (6C) fit to each set of two nonoverlapping π^0 candidates plus the ISR photon direction, the two tracks and the beam particles. Both π^0 candidates are constrained to the π^0 mass, and we retain the combination with the lowest $\chi^2_{KK\pi^0\pi^0}$.

IV. THE $K^+K^-\pi^+\pi^-$ FINAL STATE

A. Final selection and backgrounds

The experimental $\chi^2_{KK\pi^+\pi^-}$ distribution for the $K^+K^-\pi^+\pi^-$ candidates is shown in Fig. 1 as points, and the open histogram is the distribution for the simulated

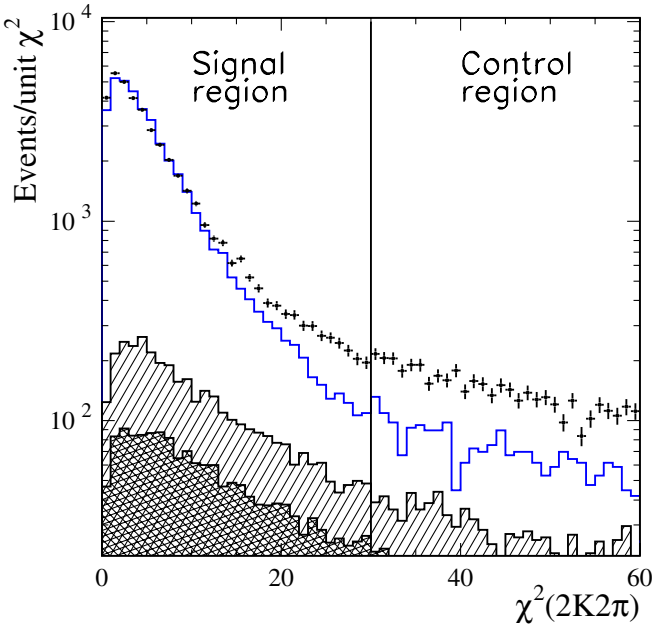

FIG. 1 (color online). Distribution of χ^2 from the three-constraint fit for $K^+K^-\pi^+\pi^-$ candidates in the data (points). The open histogram is the distribution for simulated signal events, normalized as described in the text. The cross-hatched (hatched) histogram represents the background from non-ISR events (plus that from ISR 4π events), estimated as described in the text.

$K^+K^-\pi^+\pi^-$ events. The simulated distribution is normalized to the data in the region $\chi^2_{KK\pi^+\pi^-} < 10$ where the backgrounds and radiative corrections are insignificant. The experimental distribution has contributions from background processes, but the simulated distribution is also broader than the expected 3C χ^2 distribution. This is due to multiple soft-photon emission from the initial state and radiation from the final-state charged particles, which are not taken into account by the fit, but are present in both data and simulation. The shape of the χ^2 distribution at high values was studied in detail [11,12] using specific ISR processes for which a very clean sample can be obtained without any limit on the χ^2 value.

The cross-hatched histogram in Fig. 1 represents the background from $e^+e^- \to q\bar{q}$ events, which is based on the JETSET simulation. It is dominated by events with a hard π^0 producing a fake ISR photon, and the similar kinematics cause it to peak at low values of $\chi^2_{KK\pi^+\pi^-}$. We evaluate this background in a number of $E_{\rm c.m.}$ ranges by combining the ISR photon candidate with another photon candidate in both data and simulated events, and comparing the π^0 signals in the resulting $\gamma\gamma$ invariant-mass distributions. The simulation gives an $E_{\rm c.m.}$-dependence consistent with the data, so we normalize it by an overall factor. The hatched histogram represents the sum of this background and that from ISR $e^+e^- \to \pi^+\pi^-\pi^+\pi^-$ events with one or two misidentified $\pi^\pm$, which also contributes at low χ^2 values. We estimate the contribution as a function of $E_{\rm c.m.}$ from a simulation using the known cross section [11].

All remaining background sources are either negligible or give a $\chi^2_{KK\pi^+\pi^-}$ distribution that is nearly uniform over the range shown in Fig. 1. We therefore define a signal region $\chi^2_{KK\pi^+\pi^-} < 30$, and estimate the sum of the remaining backgrounds from the difference between the number of data and simulated entries in a control region, $30 < \chi^2_{KK\pi^+\pi^-} < 60$. This difference is normalized to the corresponding difference in the signal region, as described in detail in Refs. [11,12]. The signal region contains 34635 data and 14 077 simulated events, and the control region contains 4634 data and 723 simulated events.

Figure 2 shows the $K^+K^-\pi^+\pi^-$ invariant-mass distribution from threshold up to 5.0 GeV/c^2 for events in the signal region. Narrow peaks are apparent at the J/ψ and $\psi(2S)$ masses. The cross-hatched histogram represents the $q\bar{q}$ background, which is negligible at low mass but becomes large at higher masses. The hatched region represents the ISR $\pi^+\pi^-\pi^+\pi^-$ contribution, which we estimate to be 2.4% of the selected events on average. The open histogram represents the sum of all backgrounds, including those estimated from the control region. They total 6%–8% at low mass but account for 20%–25% of the observed data near 4 GeV/c^2 and become the largest contribution near 5 GeV/c^2.

We subtract the sum of backgrounds in each mass bin to obtain a number of signal events. Considering uncertainties

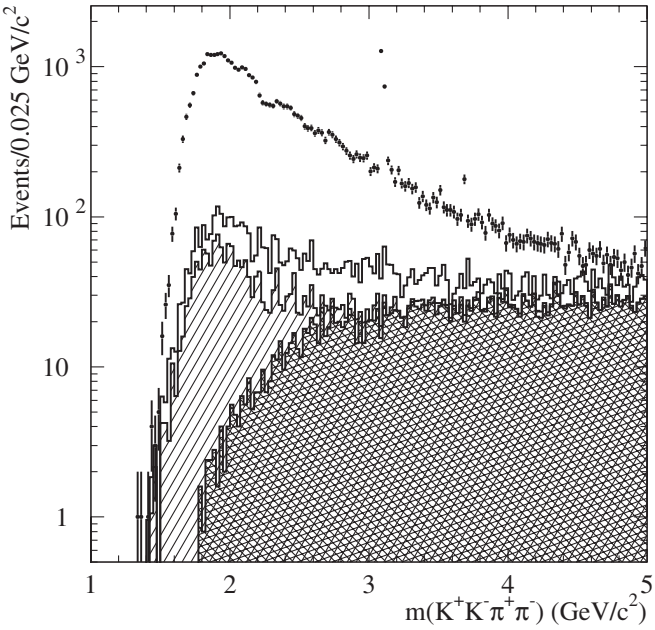

FIG. 2. The invariant-mass distribution for $K^+K^-\pi^+\pi^-$ candidates in the data (points): the cross-hatched, hatched and open histograms represent, cumulatively, the non-ISR background, the contribution from ISR $\pi^+\pi^-\pi^+\pi^-$ events, and the ISR background from the control region of Fig. 1.

in the cross sections for the background processes, the normalization of events in the control region and the simulation statistics, we estimate a systematic uncertainty on the signal yield that is less than 3% in the 1.6–3 GeV/c^2 mass region, but increases to 3%–5% in the region above 3 GeV/c^2.

B. Selection efficiency

The selection procedures applied to the data are also applied to the simulated signal samples. The resulting $K^+K^-\pi^+\pi^-$ invariant-mass distributions in the signal and control regions are shown in Fig. 3(a) for the phase space simulation. The broad, smooth mass distribution is chosen to facilitate the estimation of the efficiency as a function of mass, and this model reproduces the observed distributions of kaon and pion momenta and polar angles. We divide the number of reconstructed simulated events in each mass interval by the number generated in that interval to obtain the efficiency shown as the points in Fig. 3(b). The 3rd order polynomial fit to the points is used for further calculations. We simulate events with the ISR photon confined to the angular range 20°–160° with respect to the electron beam in the e^+e^- c.m. frame, which is about 30% wider than the EMC acceptance. This efficiency is for this fiducial region, but includes the acceptance for the final-state hadrons, the inefficiencies of the detector subsystems, and event loss due to additional soft-photon emission.

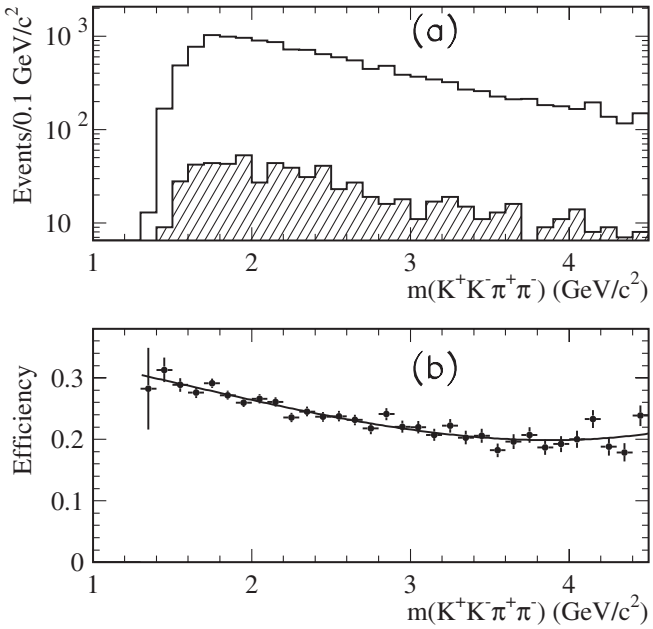

FIG. 3. (a) The invariant-mass distributions for simulated $K^+K^-\pi^+\pi^-$ events in the phase space model, reconstructed in the signal (open) and control (hatched) regions of Fig. 1; (b) net reconstruction and selection efficiency as a function of mass obtained from this simulation (the curve represents a 3rd order polynomial fit).

The simulations including the $\phi(1020)\pi^+\pi^-$ and/or $K^+K^-f_0(980)$ channels have very different mass and angular distributions in the $K^+K^-\pi^+\pi^-$ rest frame. However, the angular acceptance is quite uniform for ISR events, and the efficiencies are consistent with those from the phase space simulation within 3%. To study possible mismodeling of the acceptance, we repeat the analysis with the tighter requirements that all charged tracks be within the DIRC acceptance, $0.45 < \theta_{\rm ch} < 2.4$ radians, and the ISR photon be well away from the edges of the EMC, $0.35 < \theta_{\rm ISR} < 2.4$ radians. The fraction of selected data events satisfying the tighter requirements differs from the simulated ratio by 3.7%. We conservatively take the sum in quadrature of this variation and the 3% model variation (5% total) as a systematic uncertainty due to acceptance and model dependence.

We correct for mismodeling of the shape of the $\chi^2_{KK\pi^+\pi^-}$ distribution by $(3.0 \pm 2.0)\%$ and the track-finding efficiency following the procedures described in detail in Ref. [11]. We use a comparison of data and simulated $\chi^2_{4\pi}$ distributions in the much larger samples of ISR $\pi^+\pi^-\pi^+\pi^-$ events. We consider data and simulated events that contain a high-energy photon plus exactly three charged tracks and satisfy a set of kinematical criteria, including a good χ^2 from a kinematic fit under the hypothesis that there is exactly one missing track in the event. We find that the simulated track-finding efficiency is overestimated by $(0.8 \pm 0.5)\%$ per track, so we apply a correction of $+(3 \pm 2)\%$ to the signal yield.

We correct the simulated kaon identification efficiency using $e^+e^- \to \phi(1020)\gamma \to K^+K^-\gamma$ events. Events with a hard ISR photon and two charged tracks, one of which is identified as a kaon, with a K^+K^- invariant mass near the ϕ mass provide a very clean sample, and we compare the fractions of data and simulated events with the other track also identified as a kaon, as a function of momentum. The data-simulation efficiency ratio averages 0.990 ± 0.001 in the 1–5 GeV/c momentum range with variations at the 0.01 level. We conservatively apply a correction of $+(1.0 \pm 1.0)\%$ per kaon, or $+(2.0 \pm 2.0)\%$ to the signal yield.

C. Cross section for $e^+e^- \to K^+K^-\pi^+\pi^-$

We calculate the $e^+e^- \to K^+K^-\pi^+\pi^-$ cross section as a function of the effective c.m. energy from

$$\sigma_{KK\pi^+\pi^-}(E_{\rm c.m.}) = \frac{dN_{KK\pi^+\pi^-\gamma}(E_{\rm c.m.})}{d\mathcal{L}(E_{\rm c.m.}) \cdot \epsilon_{KK\pi^+\pi^-}(E_{\rm c.m.})}, \qquad (2)$$

where $E_{\rm c.m.} \equiv m_{KK\pi^+\pi^-}c^2$, $m_{KK\pi^+\pi^-}$ is the measured invariant mass of the $K^+K^-\pi^+\pi^-$ system, $dN_{KK\pi^+\pi^-\gamma}$ is the number of selected events after background subtraction in the interval $dE_{\rm c.m.}$, and $\epsilon_{KK\pi^+\pi^-}(E_{\rm c.m.})$ is the corrected detection efficiency. We calculate the differential luminosity, $d\mathcal{L}(E_{\rm c.m.})$, in each interval $dE_{\rm c.m.}$ from ISR $\mu^+\mu^-\gamma$

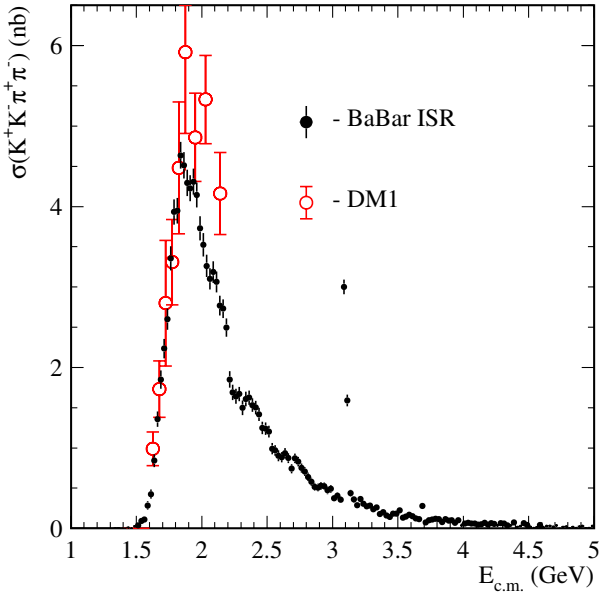

FIG. 4 (color online). The $e^+e^- \to K^+K^-\pi^+\pi^-$ cross section as a function of the effective e^+e^- c.m. energy measured with ISR data at *BABAR* (dots). The direct measurements from DM1 [13] are shown as the open circles. Only statistical errors are shown.

events with the photon in the same fiducial range used for the simulation; the procedure is described in Refs. [11,12]. From data-simulation comparison we conservatively estimate a systematic uncertainty on $d\mathcal{L}$ of 3%. This $d\mathcal{L}$ has been corrected for vacuum polarization and final-state soft-photon emission; the former should be excluded when using these data in calculations of $g_\mu - 2$.

For the cross-section measurement we use the tighter angular criteria on the charged tracks and the ISR photon, discussed in Sec. IV B, to exclude possible errors from incorrect simulation of the EMC and DCH edge effects. We show the cross section as a function of $E_{\rm c.m.}$ in Fig. 4, with statistical errors only, and provide a list of our results in Table I. The result is consistent with the direct measurement by DM1 [13], and with our previous measurement of this channel [11] but has much better statistical precision. The systematic uncertainties, summarized in Table II, affect the normalization, but have little effect on the energy dependence.

The cross section rises from threshold to a peak value of about 4.7 nb near 1.85 GeV, then generally decreases with increasing energy. In addition to narrow peaks at the J/ψ and $\psi(2S)$ masses, there are several possible wider struc-

TABLE I. Measurements of the $e^+e^- \to K^+K^-\pi^+\pi^-$ cross section (errors are statistical only).

$E_{\rm c.m.}$ (GeV)	σ (nb)	$E_{\rm c.m.}$ (GeV)	σ (nb)	$E_{\rm c.m.}$ (GeV)	σ (nb)	$E_{\rm c.m.}$ (GeV)	σ (nb)	$E_{\rm c.m.}$ (GeV)	σ (nb)
1.4125	0.00 ± 0.02	2.1375	2.83 ± 0.13	2.8625	0.50 ± 0.05	3.5875	0.12 ± 0.03	4.3125	0.04 ± 0.02
1.4375	0.01 ± 0.02	2.1625	2.71 ± 0.12	2.8875	0.51 ± 0.05	3.6125	0.13 ± 0.03	4.3375	0.04 ± 0.02
1.4625	0.00 ± 0.02	2.1875	2.46 ± 0.12	2.9125	0.54 ± 0.05	3.6375	0.12 ± 0.03	4.3625	0.03 ± 0.02
1.4875	0.04 ± 0.02	2.2125	1.84 ± 0.10	2.9375	0.46 ± 0.05	3.6625	0.11 ± 0.03	4.3875	0.06 ± 0.02
1.5125	0.03 ± 0.02	2.2375	1.66 ± 0.10	2.9625	0.45 ± 0.05	3.6875	0.25 ± 0.03	4.4125	0.01 ± 0.02
1.5375	0.11 ± 0.03	2.2625	1.59 ± 0.09	2.9875	0.46 ± 0.05	3.7125	0.07 ± 0.03	4.4375	0.03 ± 0.02
1.5625	0.15 ± 0.04	2.2875	1.66 ± 0.09	3.0125	0.36 ± 0.04	3.7375	0.08 ± 0.02	4.4625	0.06 ± 0.02
1.5875	0.32 ± 0.05	2.3125	1.50 ± 0.09	3.0375	0.39 ± 0.04	3.7625	0.11 ± 0.03	4.4875	0.03 ± 0.02
1.6125	0.48 ± 0.06	2.3375	1.65 ± 0.09	3.0625	0.31 ± 0.04	3.7875	0.11 ± 0.03	4.5125	0.04 ± 0.02
1.6375	0.85 ± 0.08	2.3625	1.56 ± 0.09	3.0875	2.95 ± 0.10	3.8125	0.10 ± 0.03	4.5375	0.01 ± 0.02
1.6625	1.42 ± 0.10	2.3875	1.49 ± 0.09	3.1125	1.51 ± 0.08	3.8375	0.08 ± 0.02	4.5625	0.02 ± 0.02
1.6875	1.86 ± 0.11	2.4125	1.46 ± 0.09	3.1375	0.37 ± 0.04	3.8625	0.12 ± 0.03	4.5875	0.05 ± 0.02
1.7125	2.36 ± 0.13	2.4375	1.48 ± 0.09	3.1625	0.35 ± 0.04	3.8875	0.09 ± 0.02	4.6125	0.02 ± 0.02
1.7375	2.67 ± 0.13	2.4625	1.17 ± 0.08	3.1875	0.28 ± 0.04	3.9125	0.09 ± 0.02	4.6375	0.01 ± 0.02
1.7625	3.51 ± 0.15	2.4875	1.16 ± 0.08	3.2125	0.35 ± 0.04	3.9375	0.08 ± 0.02	4.6625	0.04 ± 0.02
1.7875	3.98 ± 0.16	2.5125	1.21 ± 0.08	3.2375	0.31 ± 0.04	3.9625	0.10 ± 0.02	4.6875	0.02 ± 0.02
1.8125	4.10 ± 0.16	2.5375	0.94 ± 0.07	3.2625	0.30 ± 0.04	3.9875	0.04 ± 0.02	4.7125	0.03 ± 0.02
1.8375	4.68 ± 0.17	2.5625	0.95 ± 0.07	3.2875	0.24 ± 0.04	4.0125	0.06 ± 0.02	4.7375	0.01 ± 0.02
1.8625	4.49 ± 0.17	2.5875	0.84 ± 0.07	3.3125	0.22 ± 0.04	4.0375	0.07 ± 0.02	4.7625	0.02 ± 0.02
1.8875	4.26 ± 0.17	2.6125	0.85 ± 0.07	3.3375	0.25 ± 0.04	4.0625	0.05 ± 0.02	4.7875	0.01 ± 0.02
1.9125	4.30 ± 0.16	2.6375	0.90 ± 0.07	3.3625	0.16 ± 0.03	4.0875	0.06 ± 0.02	4.8125	0.00 ± 0.02
1.9375	4.20 ± 0.16	2.6625	0.82 ± 0.06	3.3875	0.17 ± 0.03	4.1125	0.06 ± 0.02	4.8375	0.02 ± 0.02
1.9625	4.13 ± 0.16	2.6875	0.70 ± 0.06	3.4125	0.18 ± 0.03	4.1375	0.05 ± 0.02	4.8625	0.00 ± 0.02
1.9875	3.74 ± 0.15	2.7125	0.86 ± 0.06	3.4375	0.12 ± 0.03	4.1625	0.06 ± 0.02	4.8875	0.04 ± 0.02
2.0125	3.45 ± 0.15	2.7375	0.81 ± 0.06	3.4625	0.17 ± 0.03	4.1875	0.05 ± 0.02	4.9125	0.05 ± 0.02
2.0375	3.38 ± 0.14	2.7625	0.76 ± 0.06	3.4875	0.17 ± 0.03	4.2125	0.05 ± 0.02	4.9375	0.02 ± 0.02
2.0625	3.17 ± 0.14	2.7875	0.73 ± 0.06	3.5125	0.21 ± 0.03	4.2375	0.08 ± 0.02	4.9625	0.00 ± 0.02
2.0875	3.23 ± 0.14	2.8125	0.64 ± 0.05	3.5375	0.14 ± 0.03	4.2625	0.04 ± 0.02	4.9875	0.04 ± 0.02
2.1125	3.15 ± 0.14	2.8375	0.56 ± 0.05	3.5625	0.16 ± 0.03	4.2875	0.08 ± 0.02		

TABLE II. Summary of corrections and systematic uncertainties on the $e^+e^- \to K^+K^-\pi^+\pi^-$ cross section. The total correction is the linear sum of the components and the total uncertainty is the sum in quadrature.

Source	Correction	Uncertainty
Radiative corrections	···	1%
Backgrounds	···	3%, $m_{KK\pi^+\pi^-} < 3$ GeV/c^2
		5%, $m_{KK\pi^+\pi^-} > 3$ GeV/c^2
Model dependence	···	5%
$\chi^2_{KK\pi^+\pi^-}$ Distribution	+3%	2%
Tracking efficiency	+3%	2%
Kaon ID efficiency	+2%	2%
ISR luminosity	···	3%
Total	+8%	7%, $m_{KK\pi^+\pi^-} < 3$ GeV/c^2
		9%, $m_{KK\pi^+\pi^-} > 3$ GeV/c^2

tures in the 1.8–2.8 GeV region. Such structures might be due to thresholds for intermediate resonant states, such as $\phi f_0(980)$ near 2 GeV. Gaussian fits to the simulated line shapes give a resolution on the measured $K^+K^-\pi^+\pi^-$ mass that varies between 4.2 MeV/c^2 in the 1.5–2.5 GeV/c^2 region and 5.5 MeV/c^2 in the 2.5–3.5 GeV/c^2 region. The resolution function is not purely Gaussian due to soft-photon radiation, but less than 10% of the signal is outside the 25 MeV/c^2 mass bin. Since the cross section has no sharp structure other than the J/ψ and $\psi(2S)$ peaks discussed in Sec. VIII below, we apply no correction for resolution.

D. Substructure in the $K^+K^-\pi^+\pi^-$ final state

Our previous study [11] showed many intermediate resonances in the $K^+K^-\pi^+\pi^-$ final state. With the larger data sample used here, they can be seen more clearly and, in some cases, studied in detail. Figure 5(a) shows a scatter plot of the invariant mass of the $K^-\pi^+$ pair versus that of the $K^+\pi^-$ pair, and Fig. 5(b) shows the sum of the two projections. Here we have suppressed the contributions from $\phi\pi^+\pi^-$ and $K^+K^-\rho(770)$ by requiring $|m(K^+K^-) - m(\phi)| > 10$ MeV/c^2 and $|m(\pi^+\pi^-) - m(\rho)| > 100$ MeV/c^2, where $m(\phi)$ and $m(\rho)$ values are taken from the Particle Data Group (PDG) tables [5]. Bands and peaks corresponding to the $K^{*0}(892)$ and $K_2^{*0}(1430)$ are visible. In Fig. 5(c) we show the sum of projections of the $K^{*0}(892)$ bands, defined by lines in Fig. 5(a), with events in the overlap region plotted only once. No $K^{*0}(892)$ signal is seen, confirming that the $e^+e^- \to K^{*0}(892)\bar{K}^{*0}(892)$ cross section is small. We observe associated $K^{*0}(892)\bar{K}_2^{*0}(1430)$ production, but it is mostly from J/ψ decays (see Sec. VIII).

We combine $K^{*0}/\bar{K}^{*0}$ candidates within the lines in Fig. 5(a) with the remaining pion and kaon to obtain the $K^{*0}\pi^{+-}$ invariant-mass distribution shown in Fig. 6(a), and the $K^{*0}\pi^{+-}$ vs $K^{*0}K^{-+}$ mass scatter plot in Fig. 6(b). The bulk of Fig. 6(b) shows a strong positive

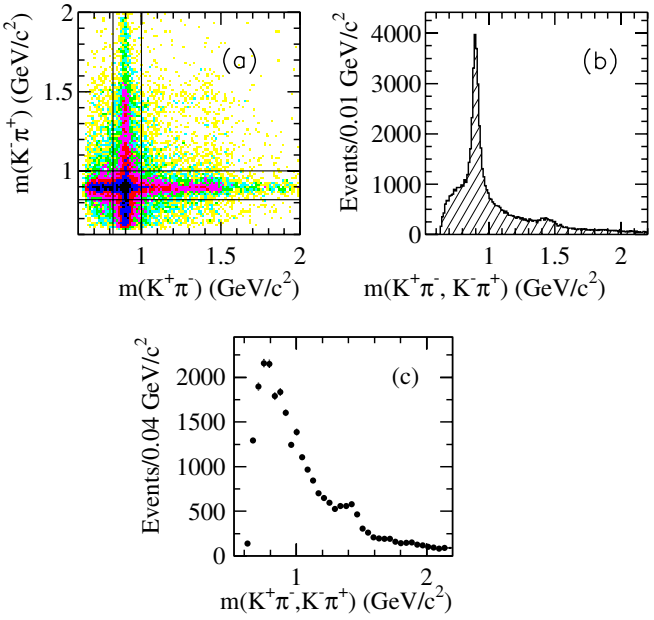

FIG. 5 (color online). (a) Invariant mass of the $K^-\pi^+$ pair versus that of the $K^+\pi^-$ pair; (b) sum of projections of (a); (c) sum of projections of the K^{*0} bands of (a), with events in the overlap region taken only once. The $\phi\pi^+\pi^-$ and $KK\rho$ are vetoed.

correlation, characteristic of $K^{*0}K\pi$ final states with no higher resonances. The horizontal band in Fig. 6(b) corresponds to the peak region in Fig. 6(a), and is consistent with contributions from the $K_1(1270)$ and $K_1(1400)$ resonances. There is also an indication of a vertical band in Fig. 6(b), perhaps corresponding to a $K^{*0}K$ resonance at $\sim$1.5 GeV/c^2.

We now suppress $K^{*0}K\pi$ by considering only events outside the lines in Fig. 5(a). In Fig. 7 we show the $K^\pm\pi^+\pi^-$ invariant mass (two entries per event) vs that of the $\pi^+\pi^-$ pair, along with its two projections. There is a strong $\rho(770) \to \pi^+\pi^-$ signal, and the $K^\pm\pi^+\pi^-$ mass projection shows further indications of the $K_1(1270)$ and $K_1(1400)$ resonances, both of which decay into $K\rho(770)$. There are suggestions of additional structure in the $\pi^+\pi^-$ mass distribution, including possible $f_0(980)$ shoulder and

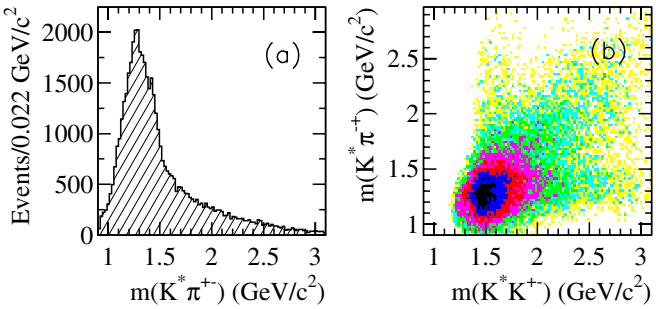

FIG. 6 (color online). (a) The $K^{*0}\pi$ invariant-mass distribution; (b) the $K^{*0}\pi$ mass versus $K^{*0}K$ mass.

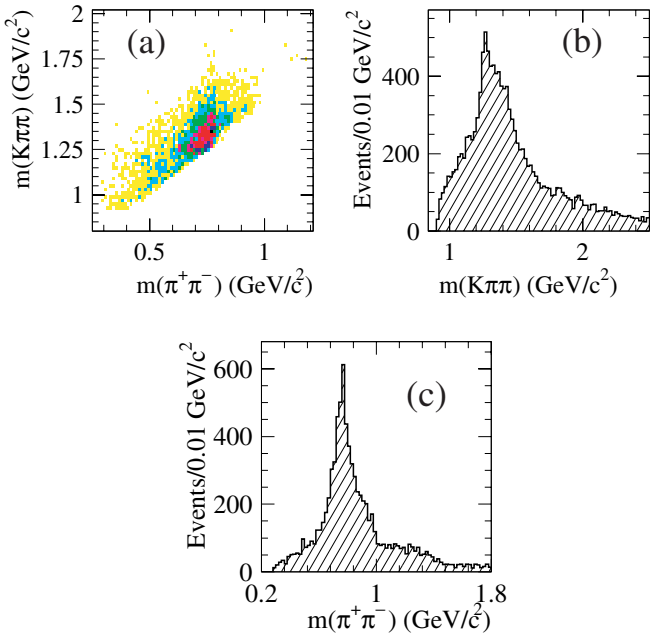

FIG. 7 (color online). (a) Invariant mass of the $K^{\pm}\pi^{+}\pi^{-}$ combinations versus that of the $\pi^{+}\pi^{-}$ pair; (b) the $K^{\pm}\pi^{+}\pi^{-}$ and (c) $\pi^{+}\pi^{-}$ mass projections of (a).

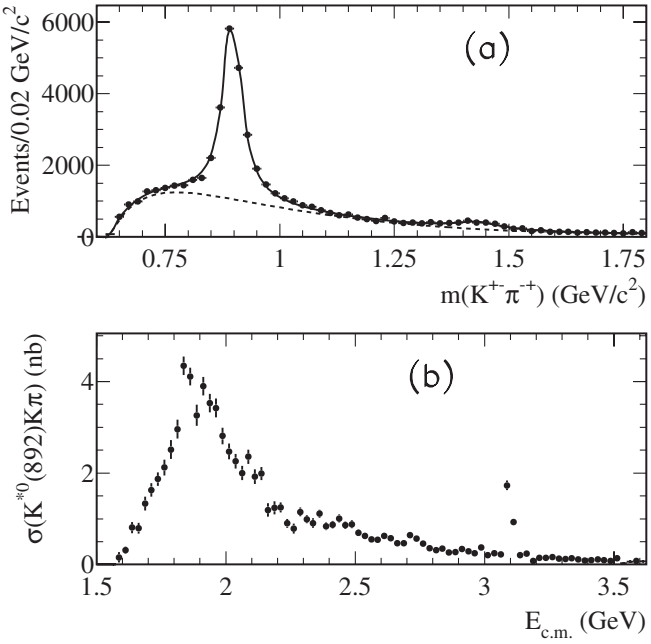

FIG. 8. (a) The $K^{\pm}\pi^{\mp}$ mass distribution (two entries per event) for all selected $K^{+}K^{-}\pi^{+}\pi^{-}$ events: the solid line represents a fit including two resonances and a polynomial function (see text), shown separately as the dashed line; (b) the $e^{+}e^{-} \to K^{*0}K\pi$ cross section obtained from the $K^{*0}(892)$ signal by a similar fit in each 25 MeV$/c^2$ mass bin.

a possible enhancement near the $f_2(1270)$, however the current statistics do not allow us to make definitive statements.

The separation of all these, and any other, intermediate states involving relatively wide resonances requires a partial wave analysis. This is beyond the scope of this paper. Here we present the cross section for the sum of all states including a $K^{*0}(892)$, and study intermediate states that include a narrow ϕ or f_0 resonance.

E. The $e^{+}e^{-} \to K^{*0}K\pi$ cross section

Signals for the $K^{*0}(892)$ and $K_2^{*0}(1430)$ are clearly visible in the $K^{\pm}\pi^{\mp}$ mass distributions in Fig. 5(b) and, with a different bin size, in Fig. 8(a). We perform a fit to this distribution using P-wave Breit-Wigner (BW) functions for the K^{*0} and K_2^{*0} signals and a third-order polynomial function for the remainder of the distribution taking into account the $K\pi$ threshold. The result is shown in Fig. 8(a). The fit yields a K^{*0} signal of 19738 $\pm$ 266 events with $m(K\pi) = 896.2 \pm 0.3$ MeV$/c^2$ and $\Gamma(K\pi) = 50.6 \pm 0.9$ MeV, and a K_2^{*0} signal of 1786 $\pm$ 127 events with $m(K\pi) = 1428.5 \pm 3.9$ MeV$/c^2$ and $\Gamma(K\pi) = 113.7 \pm 9.2$ MeV. These values are consistent with current world averages [5], and the fit describes the data well, indicating that contributions from any other resonances decaying into $K^{\pm}\pi^{\mp}$ are small.

We perform a similar fit to the data in bins of the $K^{+}K^{-}\pi^{+}\pi^{-}$ invariant mass, with the resonance masses and widths fixed to the values obtained by the overall fit. Since there is at most one K^{*0} per event, we convert the resulting K^{*0} yield in each bin into an "inclusive" $e^{+}e^{-} \to K^{*0}K\pi$ cross section, following the procedure described in Sec. IV C. This cross section is shown in Fig. 8(b) and listed in Table III for the effective c.m. energies from threshold up to 3.5 GeV. At higher energies the signals are small and contain an unknown, but possibly large, contribution from $e^{+}e^{-} \to q\bar{q}$ events. There is a rapid rise from threshold to a peak value of about 4 nb at 1.84 GeV, followed by a very rapid decrease with increasing energy. There are suggestions of narrow structure in the peak region, but the only statistically significant structure is the J/ψ peak, which is discussed below.

The $e^{+}e^{-} \to K^{*0}K\pi$ contribution is a large fraction of the total $K^{+}K^{-}\pi^{+}\pi^{-}$ cross section at all energies above its threshold, and dominates in the 1.8–2.0 GeV region. We are unable to extract a meaningful measurement of the $K_2^{*0}K\pi$ cross section from this data sample because it is more than 10 times smaller. The $K^{+}K^{-}\rho^{0}(770)$ intermediate state makes up the majority of the remainder of the cross section and it can be estimated as a difference of the values in Tables I and III for the $K^{+}K^{-}\pi^{+}\pi^{-}$ and $K^{*0}K\pi$ final states.

F. The $\phi(1020)\pi^{+}\pi^{-}$ intermediate state

Intermediate states containing relatively narrow resonances can be studied more easily. Figure 9(a) shows a scatter plot of the invariant mass of the $\pi^{+}\pi^{-}$ pair versus that of the $K^{+}K^{-}$ pair. Horizontal and vertical bands

TABLE III. Measurements of the $e^+e^- \to K^{*0}(892)K\pi$ cross section (errors are statistical only).

$E_{\rm c.m.}$ (GeV)	σ (nb)	$E_{\rm c.m.}$ (GeV)	σ (nb)	$E_{\rm c.m.}$ (GeV)	σ (nb)	$E_{\rm c.m.}$ (GeV)	σ (nb)
1.5875	0.16 ± 0.11	2.0875	2.36 ± 0.16	2.5875	0.54 ± 0.07	3.0875	1.73 ± 0.10
1.6125	0.31 ± 0.08	2.1125	1.92 ± 0.16	2.6125	0.63 ± 0.06	3.1125	0.92 ± 0.07
1.6375	0.81 ± 0.13	2.1375	1.99 ± 0.14	2.6375	0.57 ± 0.06	3.1375	0.21 ± 0.04
1.6625	0.79 ± 0.12	2.1625	1.19 ± 0.15	2.6625	0.46 ± 0.06	3.1625	0.24 ± 0.04
1.6875	1.33 ± 0.15	2.1875	1.24 ± 0.14	2.6875	0.46 ± 0.06	3.1875	0.08 ± 0.03
1.7125	1.63 ± 0.15	2.2125	1.25 ± 0.11	2.7125	0.64 ± 0.06	3.2125	0.15 ± 0.03
1.7375	1.87 ± 0.14	2.2375	0.90 ± 0.10	2.7375	0.56 ± 0.06	3.2375	0.14 ± 0.04
1.7625	2.12 ± 0.17	2.2625	0.79 ± 0.11	2.7625	0.46 ± 0.06	3.2625	0.16 ± 0.03
1.7875	2.51 ± 0.20	2.2875	1.15 ± 0.10	2.7875	0.36 ± 0.06	3.2875	0.13 ± 0.03
1.8125	2.96 ± 0.21	2.3125	0.99 ± 0.09	2.8125	0.31 ± 0.05	3.3125	0.12 ± 0.03
1.8375	4.35 ± 0.20	2.3375	0.91 ± 0.11	2.8375	0.35 ± 0.05	3.3375	0.14 ± 0.03
1.8625	4.11 ± 0.20	2.3625	1.11 ± 0.09	2.8625	0.27 ± 0.04	3.3625	0.12 ± 0.06
1.8875	3.26 ± 0.23	2.3875	0.83 ± 0.09	2.8875	0.27 ± 0.05	3.3875	0.09 ± 0.03
1.9125	3.90 ± 0.20	2.4125	0.87 ± 0.09	2.9125	0.34 ± 0.05	3.4125	0.10 ± 0.03
1.9375	3.53 ± 0.20	2.4375	1.00 ± 0.09	2.9375	0.29 ± 0.04	3.4375	0.11 ± 0.03
1.9625	3.42 ± 0.21	2.4625	0.86 ± 0.08	2.9625	0.25 ± 0.04	3.4625	0.10 ± 0.05
1.9875	2.81 ± 0.18	2.4875	0.88 ± 0.09	2.9875	0.38 ± 0.05	3.4875	0.08 ± 0.03
2.0125	2.47 ± 0.17	2.5125	0.69 ± 0.07	3.0125	0.21 ± 0.04		
2.0375	2.26 ± 0.16	2.5375	0.62 ± 0.07	3.0375	0.24 ± 0.04		
2.0625	2.00 ± 0.16	2.5625	0.55 ± 0.07	3.0625	0.22 ± 0.04		

corresponding to the $\rho^0(770)$ and ϕ, respectively, are visible, and there is a concentration of entries on the ϕ band corresponding to the correlated production of ϕ and $f_0(980)$. The ϕ signal is also visible in the K^+K^- mass projection, Fig. 9(c). The large contribution from the $\rho(770)$, coming from the K_1 decay, is nearly uniform in the K^+K^- mass, and the cross-hatched histogram shows the non-$K^+K^-\pi^+\pi^-$ background estimated from the control region in $\chi^2_{KK\pi^+\pi^-}$. The cross-hatched histogram also shows a ϕ peak, but this is a small fraction of the events. Subtracting this background and fitting the remaining data gives 1706 ± 56 events produced via the $\phi\pi^+\pi^-$ intermediate state.

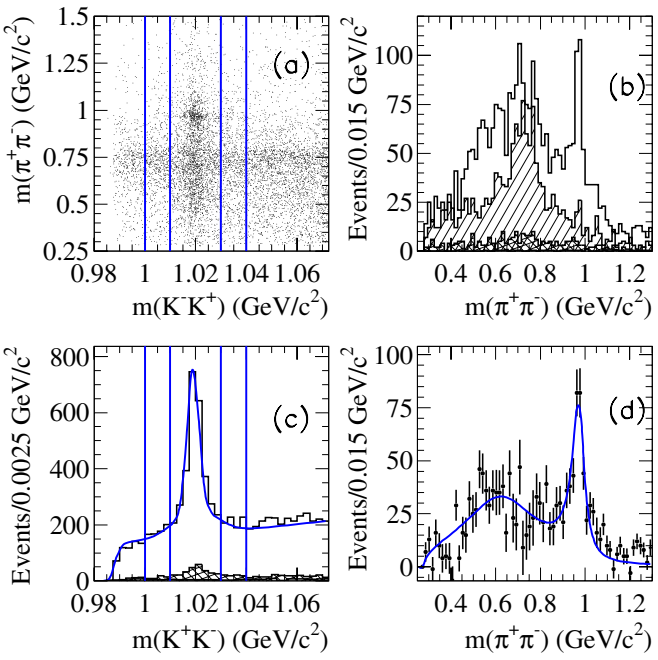

FIG. 9 (color online). (a) The $\pi^+\pi^-$ vs the K^+K^- invariant masses for all selected $K^+K^-\pi^+\pi^-$ events; (b) the $\pi^+\pi^-$ invariant-mass projections for events in the ϕ peak (open histogram), sidebands (hatched) and background control region (cross-hatched); (c) the K^+K^- mass projections for all events (open) and control region (cross-hatched); (d) the difference between the open and the sum of the other histograms in (b).

To study the $\phi\pi^+\pi^-$ channel, we select candidate events with a K^+K^- invariant mass within 10 MeV/c^2 of the ϕ mass, indicated by the inner vertical lines in Figs. 9(a) and 9(c), and estimate the non-ϕ contribution from the mass sidebands between the inner and outer vertical lines. In Fig. 9(b) we show the $\pi^+\pi^-$ invariant-mass distributions for ϕ candidate events, sideband events and χ^2 control region events as the open, hatched and cross-hatched histograms, respectively, and in Fig. 9(d) we show the numbers of entries from the candidate events minus those from the sideband and control region. There is a clear f_0 peak over a broad mass distribution, with no indication of associated ρ^0 production.

A coherent sum of two Breit-Wigner functions is sufficient to describe the invariant-mass distribution of the $\pi^+\pi^-$ pair recoiling against a ϕ in Fig. 9(d). We fit with the function:

$$F(m) = \sqrt{1 - 4m_\pi^2/m^2} \cdot |A_1(m) + e^{i\psi}A_2(m)|^2,$$
$$A_i(m) = m_i\Gamma_i\sqrt{N_i}/(m_i^2 - m^2 + im_i\Gamma_i), \quad (3)$$

where m is the $\pi^+\pi^-$ invariant mass, m_i and Γ_i are the parameters of the ith resonance, ψ is their relative phase and N_i are normalization parameters, corresponding to the number of events under each BW. One BW corresponds to the $f_0(980)$, but a wide range of values of the other parameters can describe the data. Fixing the relative phase to $\psi = \pi$ and the parameters of the first BW to $m_1 = 0.6\ \mathrm{GeV}/c^2$ and $\Gamma_1 = 0.45$ GeV [which could be interpreted as the $f_0(600)$ [5]], we obtain the fit shown in Fig. 9(d). It describes the data well and gives an $f_0(980)$ signal of 262 ± 30 events, with $m_2 = 0.973 \pm 0.003\ \mathrm{GeV}/c^2$ and $\Gamma_2 = 0.065 \pm 0.013$ GeV, consistent with the PDG values [5]. There is a suggestion of an $f_2(1270)$ peak in the data, but it is much smaller than the f_0 peak and we do not consider it further.

We obtain the number of $e^+e^- \to \phi\pi^+\pi^-$ events in bins of $\phi\pi^+\pi^-$ invariant mass by fitting the K^+K^- invariant mass projection in that bin after subtracting non-$K^+K^-\pi^+\pi^-$ background. Each projection is a subset of Fig. 9(c), where the curve represents a fit to the full sample. In each mass bin, all parameters are fixed to the values obtained from the overall fit except the numbers of events in the ϕ peak and the non-ϕ component.

The efficiency may depend on the details of the production mechanism. Using the two-pion mass distribution in Fig. 9(d) as input, we simulate the $\pi^+\pi^-$ system as an S-wave comprising two scalar resonances, with parameters set to the values given above. To describe the $\phi\pi^+\pi^-$ mass distribution we use a simple model with one resonance, the $\phi(1680)$, of mass $1.68\ \mathrm{GeV}/c^2$ and width 0.2 GeV, decaying to ϕf_0. The simulated reconstructed spectrum is shown in Fig. 10(a). There is a sharp increase at about $2\ \mathrm{GeV}/c^2$ due to the $\phi f_0(980)$ threshold. All other structure is determined by phase space and a m^{-2} falloff with increasing mass.

Dividing the number of reconstructed events in each bin by the number of generated ones, we obtain the efficiency as a function of $\phi\pi^+\pi^-$ mass shown in Fig. 10(b). The solid line represents a fit to a third-order polynomial, and the dashed line the corresponding fit to the phase space model from Fig. 3. The model dependence is weak, giving confidence in the efficiency calculation. We calculate the $e^+e^- \to \phi\pi^+\pi^-$ cross section as described in Sec. IV C but using the efficiency from the fit to Fig. 10(b) and dividing by the $\phi \to K^+K^-$ branching fraction of 0.491 [5]. We show our results as a function of energy in Fig. 11 and list them in Table IV. The cross section has a peak value of about 0.6 nb at about 1.7 GeV, then decreases with increasing energy until $\phi(1020)f_0(980)$ threshold, around 2.0 GeV. From this point it rises, falls sharply at about 2.2 GeV, and then decreases slowly. Except in the charmonium region, the results at energies above 2.9 GeV are not meaningful due to small signals and potentially large backgrounds, and are omitted from Table IV. Figure 11 displays the cross section up to 4.5 GeV to show the signals from the

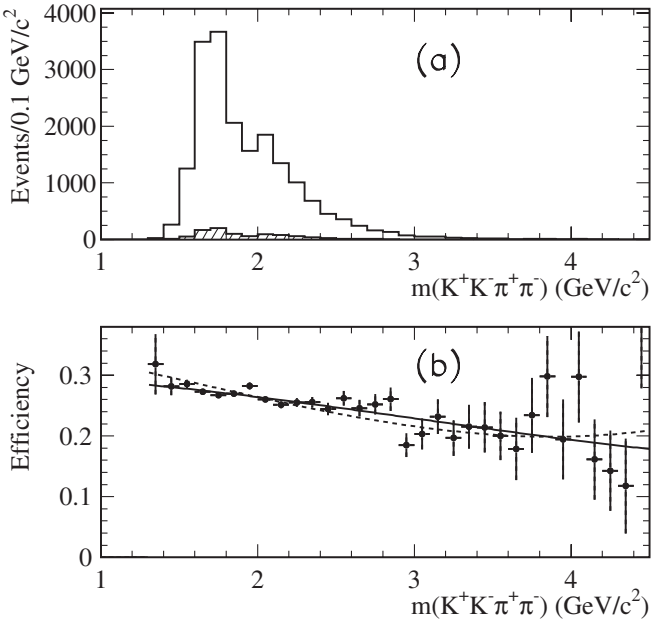

FIG. 10. (a) The $K^+K^-\pi^+\pi^-$ invariant-mass distributions from the $\phi\pi^+\pi^-$ simulation described in the text, reconstructed in the signal (open) and control (hatched) regions; (b) net reconstruction and selection efficiency as a function of mass: the solid line represents a cubic fit, and the dashed line the corresponding fit for the space phase model shown in Fig. 3.

J/ψ and $\psi(2S)$ decays. They are discussed in Sec. VIII. There are no previous measurements of this cross section, and our results are consistent with the upper limits given in Ref. [13].

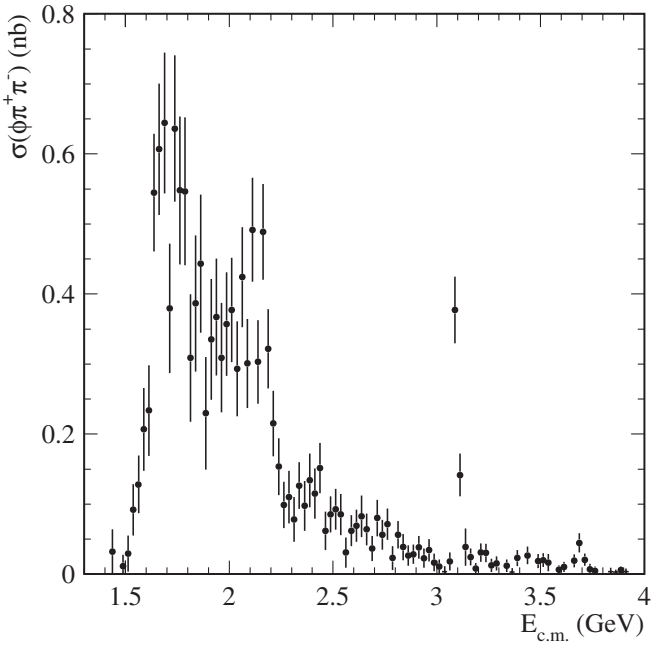

FIG. 11. The $e^+e^- \to \phi\pi^+\pi^-$ cross section as a function of the effective e^+e^- c.m. energy.

TABLE IV. Measurements of the $e^+e^- \to \phi(1020)\pi^+\pi^-$ cross section (errors are statistical only).

$E_{\rm c.m.}$ (GeV)	σ (nb)	$E_{\rm c.m.}$ (GeV)	σ (nb)	$E_{\rm c.m.}$ (GeV)	σ (nb)	$E_{\rm c.m.}$ (GeV)	σ (nb)
1.4875	0.01 ± 0.02	1.8375	0.39 ± 0.10	2.1875	0.32 ± 0.06	2.5375	0.09 ± 0.03
1.5125	0.03 ± 0.03	1.8625	0.44 ± 0.10	2.2125	0.22 ± 0.05	2.5625	0.03 ± 0.02
1.5375	0.09 ± 0.04	1.8875	0.23 ± 0.08	2.2375	0.15 ± 0.04	2.5875	0.06 ± 0.02
1.5625	0.13 ± 0.04	1.9125	0.34 ± 0.09	2.2625	0.10 ± 0.03	2.6125	0.07 ± 0.02
1.5875	0.21 ± 0.06	1.9375	0.37 ± 0.08	2.2875	0.11 ± 0.04	2.6375	0.08 ± 0.03
1.6125	0.23 ± 0.06	1.9625	0.31 ± 0.08	2.3125	0.08 ± 0.03	2.6625	0.06 ± 0.02
1.6375	0.54 ± 0.08	1.9875	0.36 ± 0.07	2.3375	0.13 ± 0.03	2.6875	0.04 ± 0.02
1.6625	0.61 ± 0.09	2.0125	0.38 ± 0.07	2.3625	0.10 ± 0.04	2.7125	0.08 ± 0.03
1.6875	0.64 ± 0.10	2.0375	0.29 ± 0.07	2.3875	0.13 ± 0.04	2.7375	0.06 ± 0.02
1.7125	0.38 ± 0.09	2.0625	0.42 ± 0.07	2.4125	0.12 ± 0.04	2.7625	0.07 ± 0.02
1.7375	0.64 ± 0.10	2.0875	0.30 ± 0.06	2.4375	0.15 ± 0.04	2.7875	0.02 ± 0.02
1.7625	0.55 ± 0.11	2.1125	0.49 ± 0.07	2.4625	0.06 ± 0.03	2.8125	0.06 ± 0.02
1.7875	0.55 ± 0.11	2.1375	0.30 ± 0.06	2.4875	0.09 ± 0.03	2.8375	0.04 ± 0.02
1.8125	0.31 ± 0.09	2.1625	0.49 ± 0.07	2.5125	0.09 ± 0.03	2.8625	0.03 ± 0.01

We perform a study of the angular distributions in the $\phi(1020)\pi^+\pi^-$ final state by considering all $K^+K^-\pi^+\pi^-$ candidate events with mass below 3 GeV/c^2, binning them in terms of the cosine of the angles defined below, and fitting the background-subtracted K^+K^- mass projections. The efficiency is nearly uniform in these angles, so we study the number of events in each bin. We define the ϕ production angle, Θ_ϕ as the angle between the ϕ momentum and the e^- beam direction in the rest frame of the $\phi\pi^+\pi^-$ system. The distribution of $\cos\Theta_\phi$, shown in Fig. 12(a), is consistent with the uniform distribution expected if S-wave two-body channels ϕX, $X \to \pi^+\pi^-$ dominate the $\phi\pi^+\pi^-$ system. We define the pion and kaon helicity angles, Θ_{π^+} and Θ_{K^+}, as those between the π^+ and the $\pi^+\pi^-$-system momenta in the $\pi^+\pi^-$ rest frame and between the K^+ and ISR photon momenta in the ϕ rest frame, respectively. The distributions of $\cos\Theta_{\pi^+}$ and $\cos\Theta_{K^+}$, shown in Figs. 12(b) and 12(c), respectively, are consistent with those expected from scalar and vector meson decays.

G. The $\phi(1020)f_0(980)$ intermediate state

The narrow $f_0(980)$ peak seen in Fig. 9(d) allows the selection of a fairly clean sample of ϕf_0 events. We repeat the analysis just described with the additional requirement that the $\pi^+\pi^-$ invariant mass be in the range 0.85–1.10 GeV/c^2. The fit to the full sample yields about 700 events; all of these contain a true ϕ, but about 10% are from $e^+e^- \to \phi\pi^+\pi^-$ events where the pion pair is not produced through the $f_0(980)$.

We convert the numbers of fitted events in each mass bin into a measurement of the $e^+e^- \to \phi(1020)f_0(980)$ cross section as described above and dividing by the $f_0 \to \pi^+\pi^-$ branching fraction of two-thirds. The cross section is shown in Fig. 13 as a function of the effective c.m. energy and is listed in Table V. Its behavior near threshold

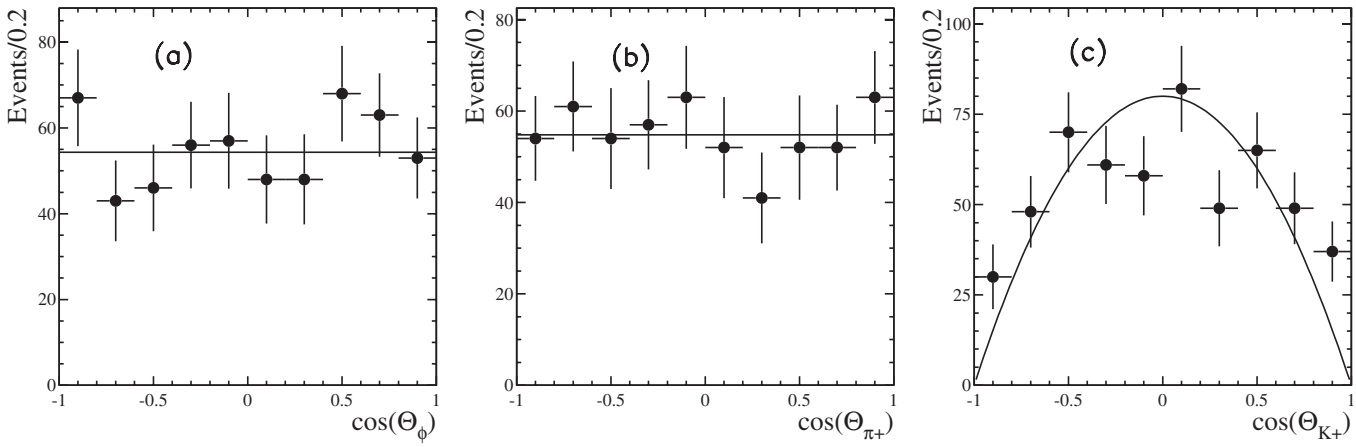

FIG. 12. Distributions of the cosines of (a) the ϕ production angle, (b) the pion helicity angle, and (c) the kaon helicity angle (see text) for $e^+e^- \to \phi\pi^+\pi^-$ events: the lines represent the distributions expected if the $\pi^+\pi^-$ system recoiling against a vector ϕ meson is produced in an S-wave, normalized to the number of events in the data.

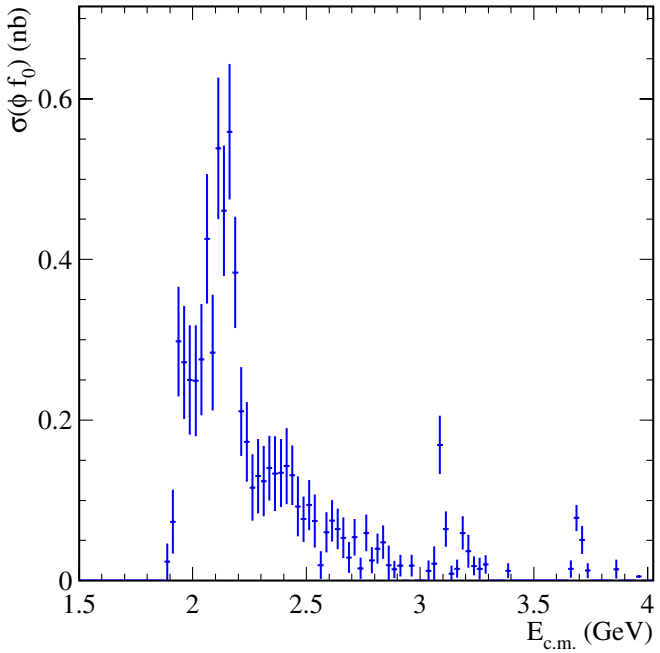

FIG. 13 (color online). The $e^+e^- \to \phi(1020)f_0(980)$ cross section as a function of the effective e^+e^- c.m. energy obtained from the $K^+K^-\pi^+\pi^-$ state.

does not appear to be smooth, but is more consistent with a steep rise to a value of about 0.3 nb at 1.95 GeV followed by a slow decrease that is interrupted by a structure around 2.175 GeV. Possible interpretations of this structure are discussed in Sec. VII. Again, the values are not meaningful for the effective c.m. above about 2.9 GeV$/c^2$, except for the J/ψ and $\psi(2S)$ signals, discussed in Sec. VIII.

V. THE $K^+K^-\pi^0\pi^0$ FINAL STATE

A. Final selection and backgrounds

The $K^+K^-\pi^0\pi^0$ sample contains background from the ISR processes $e^+e^- \to K^+K^-\pi^0\gamma$ and $K^+K^-\eta\gamma$, in which two soft-photon candidates from a machine- or detector-related background combine with the relatively energetic photons from the π^0 or η to form two fake π^0 candidates. We reduce this background using the helicity angle between each reconstructed π^0 direction and the direction of its higher-energy photon daughter calculated in its rest frame. If the cosines of both helicity angles are higher than 0.85, we remove the event.

Figure 14 shows the distribution of $\chi^2_{KK\pi^0\pi^0}$ for the remaining candidates together with the simulated $K^+K^-\pi^0\pi^0$ events. Again, the distributions are broader than those for a typical 6C χ^2 due to higher order ISR, and we normalize the histogram to the data in the region $\chi^2_{KK\pi^0\pi^0} < 10$. The cross-hatched histogram in Fig. 14 represents background from $e^+e^- \to q\bar{q}$ events, evaluated in the same way as for the $K^+K^-\pi^+\pi^-$ final state. The hatched histogram represents the sum of this background and that from ISR $\pi^+\pi^-\pi^0\pi^0$ events with both charged pions misidentified as kaons, evaluated using the simulation.

The dominant background in this case is from residual ISR $K^+K^-\pi^0$ and $K^+K^-\eta$ events, as well as ISR $K^+K^-\pi^0\pi^0\pi^0$ events. Their simulated contribution, shown as the dashed histogram in Fig. 14, is consistent with the data in the high $\chi^2_{KK\pi^0\pi^0}$ region. All other backgrounds are either negligible or distributed uniformly in $\chi^2_{KK\pi^0\pi^0}$. We define a signal region, $\chi^2_{KK\pi^0\pi^0} < 50$, containing 4425 data and 6948 simulated events, and a control region, $50 < \chi^2_{KK\pi^0\pi^0} < 100$, containing 1751 data and 848 simulated events.

Figure 15 shows the $K^+K^-\pi^0\pi^0$ invariant-mass distribution from threshold up to 5 GeV$/c^2$ for events in the signal region. The $q\bar{q}$ background (cross-hatched histogram) is negligible at low masses but forms a large fraction of the selected events above about 4 GeV$/c^2$. The ISR $\pi^+\pi^-\pi^0\pi^0$ contribution (hatched region) is negligible except in the 1.5–2.5 GeV$/c^2$ region. The sum of all other backgrounds, estimated from the control region, is the dominant contribution below 1.6 GeV$/c^2$ and non-negligible everywhere. The total background in the 1.6–2.5 GeV$/c^2$ region is 15%–20% (open histogram).

TABLE V. Measurements of the $e^+e^- \to \phi(1020)f_0(980)$ cross section (errors are statistical only).

$E_{\rm c.m.}$ (GeV)	σ (nb)	$E_{\rm c.m.}$ (GeV)	σ (nb)	$E_{\rm c.m.}$ (GeV)	σ (nb)	$E_{\rm c.m.}$ (GeV)	σ (nb)
1.8875	0.02 ± 0.03	2.1625	0.48 ± 0.09	2.4375	0.13 ± 0.04	2.7125	0.04 ± 0.02
1.9125	0.03 ± 0.05	2.1875	0.33 ± 0.07	2.4625	0.06 ± 0.04	2.7375	0.01 ± 0.01
1.9375	0.28 ± 0.08	2.2125	0.10 ± 0.06	2.4875	0.09 ± 0.03	2.7625	0.06 ± 0.02
1.9625	0.17 ± 0.07	2.2375	0.13 ± 0.05	2.5125	0.11 ± 0.03	2.7875	0.04 ± 0.02
1.9875	0.18 ± 0.08	2.2625	0.12 ± 0.04	2.5375	0.05 ± 0.03	2.8125	0.03 ± 0.02
2.0125	0.23 ± 0.08	2.2875	0.06 ± 0.05	2.5625	0.02 ± 0.02	2.8375	0.04 ± 0.02
2.0375	0.19 ± 0.07	2.3125	0.06 ± 0.04	2.5875	0.04 ± 0.03	2.8625	0.00 ± 0.02
2.0625	0.28 ± 0.08	2.3375	0.14 ± 0.04	2.6125	0.08 ± 0.03	2.8875	0.02 ± 0.01
2.0875	0.18 ± 0.08	2.3625	0.09 ± 0.05	2.6375	0.06 ± 0.03	2.9125	0.02 ± 0.01
2.1125	0.37 ± 0.09	2.3875	0.11 ± 0.04	2.6625	0.04 ± 0.03	2.9375	0.00 ± 0.00
2.1375	0.40 ± 0.08	2.4125	0.08 ± 0.04	2.6875	0.02 ± 0.02	2.9625	0.01 ± 0.01

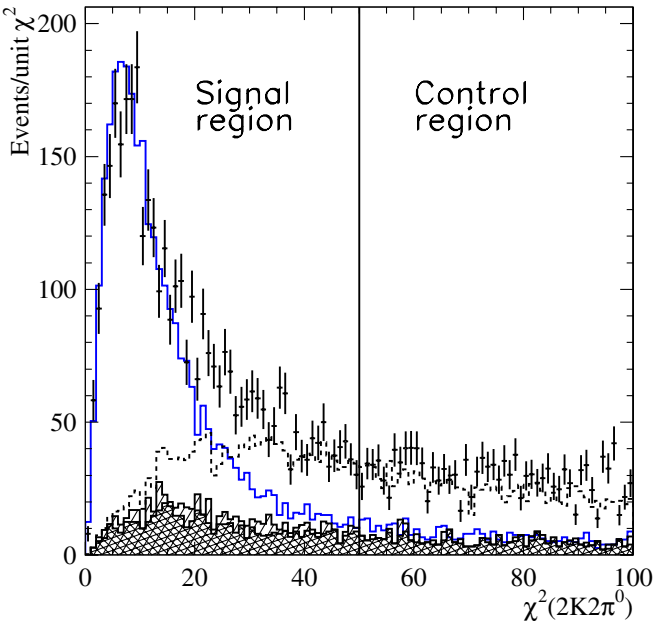

FIG. 14 (color online). Distribution of χ^2 from the six-constraint fit for $K^+K^-\pi^0\pi^0$ candidates in the data (points). The open histogram is the distribution for simulated signal events, normalized as described in the text. The cross-hatched, hatched and dashed histograms represent, cumulatively, the backgrounds from non-ISR events, ISR $\pi^+\pi^-\pi^0\pi^0$ events, and ISR $K^+K^-\pi^0$, $K^+K^-\eta$ and $K^+K^-\pi^0\pi^0\pi^0$ events.

We subtract the sum of backgrounds from the number of selected events in each mass bin to obtain a number of signal events. Considering uncertainties in the cross sections for the background processes, the normalization of events in the control region and the simulation statistics, we estimate a systematic uncertainty on the signal yield after background subtraction as less than 5% in the 1.6–3.0 GeV/c^2 region, but increases to 10% in the region above 3 GeV/c^2.

B. Selection efficiency

The detection efficiency is determined in the same manner as in Sec. IV B. Figure 16(a) shows the simulated $K^+K^-\pi^0\pi^0$ invariant-mass distributions in the signal and control regions from the phase space model. We divide the number of reconstructed events in each 40 MeV/c^2 mass interval by the number generated ones in that interval to obtain the efficiency shown as the points in Fig. 16(b); a third-order polynomial fit to the efficiency is used to calculate the cross section. Again, we simulate the ISR photon in a polar angle region wider than EMC acceptance and the efficiency shown is a factor 0.7 lower than for the hadronic system alone. Simulations assuming dominance of the $\phi \to K^+K^-$ and/or $f_0 \to \pi^0\pi^0$ channels give consistent results, and we apply the same 5% systematic uncertainty for possible model dependence as in Sec. IV B.

We correct for mismodeling of the track finding and kaon identification efficiencies as in Sec. IV B, and for the shape of the $\chi^2_{KK\pi^0\pi^0}$ distribution analogously, using

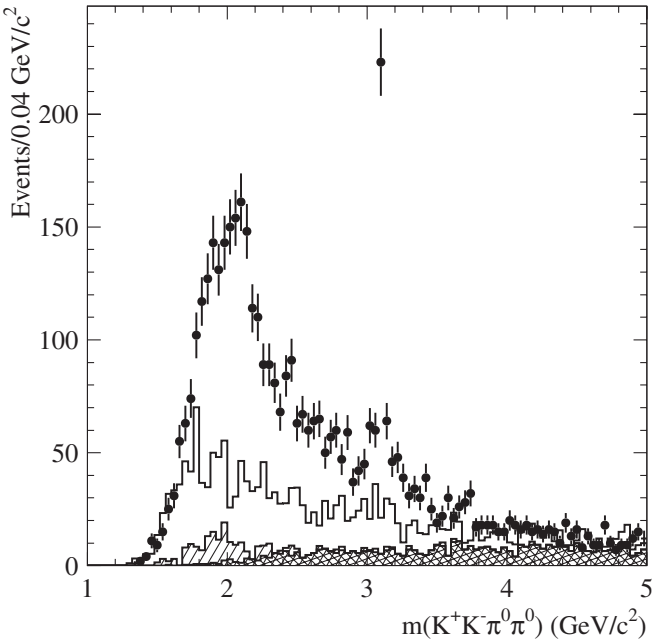

FIG. 15. Invariant-mass distribution for $K^+K^-\pi^0\pi^0$ candidates in the data (points). The cross-hatched, hatched and open histograms represent, cumulatively, the non-ISR background, the contribution from ISR $\pi^+\pi^-\pi^0\pi^0$ events, and the ISR background from the control region of Fig. 14.

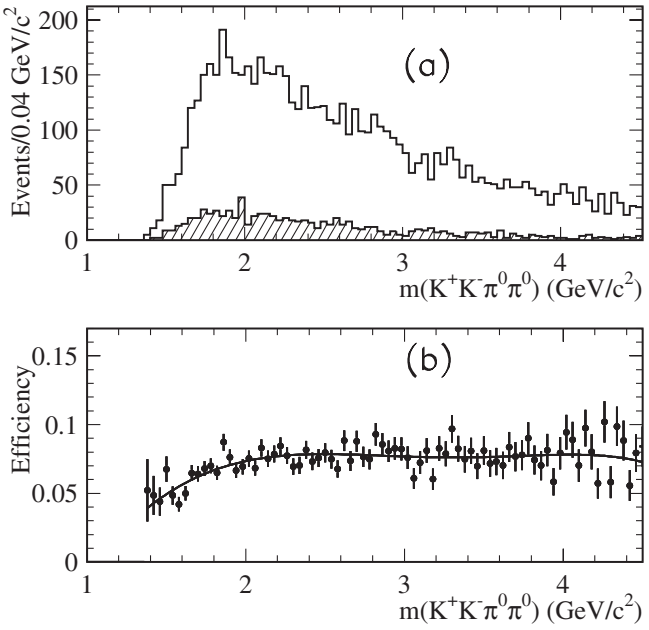

FIG. 16. (a) Invariant-mass distribution for simulated $K^+K^-\pi^0\pi^0$ events in the signal (open) and control (hatched) regions (see Fig. 14); (b) net reconstruction and selection efficiency as a function of mass obtained from this simulation (the curve represents a third-order polynomial fit).

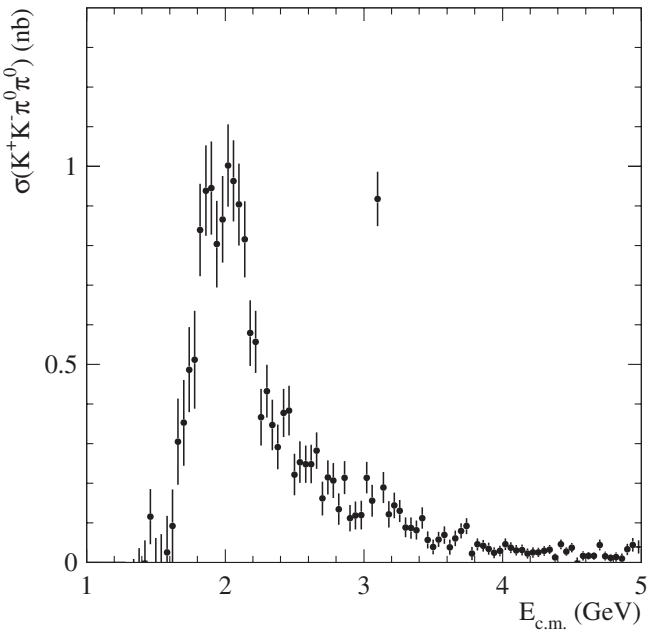

FIG. 17. The $e^+e^- \to K^+K^-\pi^0\pi^0$ cross section as a function of the effective e^+e^- c.m. energy measured with ISR data at *BABAR*. The errors are statistical only.

the result in Ref. [12], $(0 \pm 6)\%$. We correct the π^0-finding efficiency using the procedure described in detail in Ref. [12]. From ISR $e^+e^- \to \omega\pi^0\gamma \to \pi^+\pi^-\pi^0\pi^0\gamma$ events selected with and without the π^0 from the ω decay, we find that the simulated efficiency for one π^0 is too high by $(2.8 \pm 1.4)\%$. Conservatively we apply a correction of $+(5.6 \pm 2.8)\%$ for two π^0 in the event.

C. Cross section for $e^+e^- \to K^+K^-\pi^0\pi^0$

We calculate the cross section for $e^+e^- \to K^+K^-\pi^0\pi^0$ in 40 MeV $E_{\rm c.m.}$ intervals from the analog of Eq. (2), using the invariant mass of the $K^+K^-\pi^0\pi^0$ system to determine the effective c.m. energy. We show the first measurement of this cross section in Fig. 17 and list the results obtained in Table VI. The cross section rises to a peak value near 1 nb at 2 GeV, falls sharply at 2.2 GeV, then decreases slowly. The only statistically significant structure is the J/ψ peak. The drop at 2.2 GeV is similar to that seen in the $K^+K^-\pi^+\pi^-$ mode. Again, $d\mathcal{L}$ includes corrections for vacuum polarization that should be omitted from calculations of $g_\mu - 2$.

The simulated $K^+K^-\pi^0\pi^0$ invariant-mass resolution is 8.8 MeV/c^2 in the 1.5–2.5 GeV/c^2 mass range, and increases with mass to 11.2 MeV/c^2 in the 2.5–3.5 GeV/c^2 range. Since less than 20% of the events in a 40 MeV/c^2 bin are reconstructed outside that bin and the cross section has no sharp structure other than the J/ψ peak, we again make no correction for resolution. The point-to-point systematic errors are much smaller than statistical ones, and the errors on the normalization are summarized in Table VII, along with the corrections that were applied to the measurements. The total correction is +9.2%, and the

TABLE VI. Measurements of the $e^+e^- \to K^+K^-\pi^0\pi^0$ cross section (errors are statistical only).

$E_{\rm c.m.}$ (GeV)	σ (nb)	$E_{\rm c.m.}$ (GeV)	σ (nb)	$E_{\rm c.m.}$ (GeV)	σ (nb)	$E_{\rm c.m.}$ (GeV)	σ (nb)
1.4200	0.00 ± 0.05	2.3400	0.35 ± 0.06	3.2600	0.13 ± 0.03	4.1800	0.02 ± 0.01
1.4600	0.12 ± 0.07	2.3800	0.29 ± 0.06	3.3000	0.09 ± 0.03	4.2200	0.03 ± 0.01
1.5000	0.00 ± 0.07	2.4200	0.38 ± 0.06	3.3400	0.09 ± 0.03	4.2600	0.03 ± 0.01
1.5400	0.01 ± 0.08	2.4600	0.38 ± 0.06	3.3800	0.08 ± 0.02	4.3000	0.03 ± 0.01
1.5800	0.03 ± 0.09	2.5000	0.22 ± 0.05	3.4200	0.11 ± 0.03	4.3400	0.03 ± 0.01
1.6200	0.09 ± 0.09	2.5400	0.25 ± 0.05	3.4600	0.06 ± 0.02	4.3800	0.01 ± 0.01
1.6600	0.31 ± 0.11	2.5800	0.25 ± 0.05	3.5000	0.04 ± 0.02	4.4200	0.05 ± 0.01
1.7000	0.35 ± 0.11	2.6200	0.25 ± 0.05	3.5400	0.06 ± 0.02	4.4600	0.03 ± 0.01
1.7400	0.49 ± 0.11	2.6600	0.28 ± 0.05	3.5800	0.07 ± 0.02	4.5000	0.04 ± 0.01
1.7800	0.51 ± 0.12	2.7000	0.16 ± 0.04	3.6200	0.04 ± 0.02	4.5400	0.00 ± 0.01
1.8200	0.84 ± 0.12	2.7400	0.22 ± 0.04	3.6600	0.06 ± 0.02	4.5800	0.02 ± 0.01
1.8600	0.94 ± 0.11	2.7800	0.21 ± 0.04	3.7000	0.08 ± 0.02	4.6200	0.02 ± 0.01
1.9000	0.95 ± 0.12	2.8200	0.13 ± 0.04	3.7400	0.09 ± 0.02	4.6600	0.02 ± 0.01
1.9400	0.80 ± 0.11	2.8600	0.21 ± 0.04	3.7800	0.02 ± 0.02	4.7000	0.04 ± 0.01
1.9800	0.87 ± 0.11	2.9000	0.11 ± 0.03	3.8200	0.05 ± 0.01	4.7400	0.02 ± 0.01
2.0200	1.00 ± 0.10	2.9400	0.12 ± 0.04	3.8600	0.04 ± 0.01	4.7800	0.01 ± 0.01
2.0600	0.96 ± 0.10	2.9800	0.12 ± 0.04	3.9000	0.03 ± 0.02	4.8200	0.01 ± 0.01
2.1000	0.90 ± 0.10	3.0200	0.21 ± 0.04	3.9400	0.02 ± 0.01	4.8600	0.01 ± 0.01
2.1400	0.82 ± 0.10	3.0600	0.16 ± 0.04	3.9800	0.03 ± 0.01	4.9000	0.03 ± 0.01
2.1800	0.58 ± 0.08	3.1000	0.92 ± 0.07	4.0200	0.05 ± 0.01	4.9400	0.04 ± 0.02
2.2200	0.56 ± 0.08	3.1400	0.19 ± 0.04	4.0600	0.04 ± 0.01	4.9800	0.04 ± 0.02
2.2600	0.37 ± 0.07	3.1800	0.12 ± 0.03	4.1000	0.03 ± 0.01		
2.3000	0.43 ± 0.07	3.2200	0.14 ± 0.03	4.1400	0.03 ± 0.01		

TABLE VII. Summary of corrections and systematic uncertainties on the $e^+e^- \to K^+K^-\pi^0\pi^0$ cross section. The total correction is the linear sum of the components and the total uncertainty is the sum in quadrature.

Source	Correction	Uncertainty
Radiative corrections	...	1%
Backgrounds	...	5%, $m_{KK\pi^0\pi^0} < 3$ GeV/c^2
		10%, $m_{KK\pi^0\pi^0} > 3$ GeV/c^2
Model dependence	...	5%
$\chi^2_{KK\pi^0\pi^0}$ distribution	0%	6%
Tracking efficiency	+1.6%	0.8%
Kaon ID efficiency	+2%	2%
π^0 efficiency	+5.6%	2.8%
ISR luminosity	...	3%
Total	+9.2%	10%, $m_{KK\pi^0\pi^0} < 3$ GeV/c^2
		14%, $m_{KK\pi^0\pi^0} > 3$ GeV/c^2

total systematic uncertainty is 10% at low mass, increasing to 14% above 3 GeV/c^2.

D. Substructure in the $K^+K^-\pi^0\pi^0$ final state

A scatter plot of the invariant mass of the $K^-\pi^0$ versus that of the $K^+\pi^0$ pair is shown in Fig. 18(a) with two entries per event selected in the χ^2 signal region. Horizontal and vertical bands corresponding to the $K^{*+}(892)$ and $K^{*-}(892)$, respectively, are visible. Figure 18(b) shows as points the sum of the two projections of Fig. 18(a); a large $K^{*\pm}(892)$ signal is evident. Fitting this distribution with the function discussed in Sec. IV E gives a good χ^2 and the curve shown on Fig. 18(b). The $K^{*\pm}(1430)$:$K^{*\pm}(892)$ ratio is consistent with that for neutral K^* seen in the $K^+K^-\pi^+\pi^-$ channel, and the number of $K^{*\pm}(892)$ in the peak is consistent with one per selected event. The hatched histogram in Fig. 18(b) represents the $K^\pm\pi^0$ mass in events with the other $K^\mp\pi^0$ mass within the

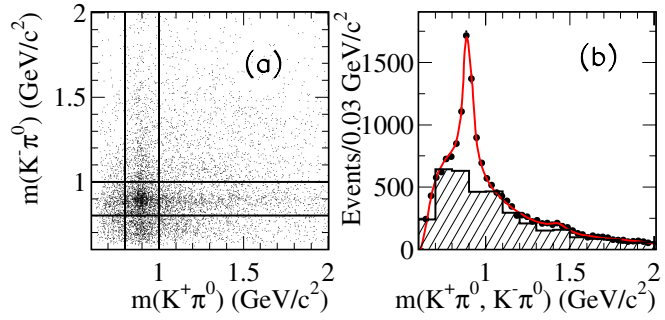

FIG. 18 (color online). (a) Invariant mass of the $K^-\pi^0$ pair versus that of the $K^+\pi^0$ pair in selected $K^+K^-\pi^0\pi^0$ events (two entries per event); (b) sum of projections of (a) (dots, four entries per event). The curve represents the result of the fit described in the text. The hatched histogram is the $K^\pm\pi^0$ distribution for events in which the other $K^\mp\pi^0$ combination is within the $K^{*\pm}(892)$ bands indicated in (a), with events in the overlap region taken only once.

lines in Fig. 18(a), but with events in the overlap region used only once, and shows no $K^{*\pm}(892)$ signal. These results indicate that the $e^+e^- \to K^{*\pm}K^{*\mp}$ cross section is small and that the $K^{*\pm}(892)K^\mp\pi^0$ channels dominate the overall cross section.

We find no signals for resonances in the $K^+K^-\pi^0$ or $K^\pm\pi^0\pi^0$ decay modes. Since the $K^{*\pm}(892)K^\mp\pi^0$ channels dominate and the statistics are low in any mass bin, we do not attempt to extract a separate $K^{*\pm}(892)K^\mp\pi^0$ cross section. The total $K^+K^-\pi^0\pi^0$ cross section is roughly a factor of 4 lower than the $K^{*0}(892)K^\pm\pi^\mp$ cross section observed in the $K^+K^-\pi^+\pi^-$ final state. This is consistent with what one might expect from isospin and the charged vs neutral K^* branching fractions into charged kaons.

E. The $\phi(1020)\pi^0\pi^0$ intermediate state

The selection of events containing a $\phi(1020) \to K^+K^-$ decay follows that in Sec. IV F. Figure 19(a) shows a scatter plot of the invariant mass of the $\pi^0\pi^0$ pair versus that of the K^+K^- pair. A vertical band corresponding to the ϕ is visible, whose intensity decreases with increasing $\pi^0\pi^0$ mass except for an enhancement in the $f_0(980)$ region. The ϕ signal is also visible in the K^+K^- invariant-mass projection shown in Fig. 19(c). The relative non-ϕ background is smaller than in the $K^+K^-\pi^+\pi^-$ mode, but there is a large background from ISR $\phi\pi^0$, $\phi\eta$ and/or $\phi\pi^0\pi^0\pi^0$ events, as indicated by the control

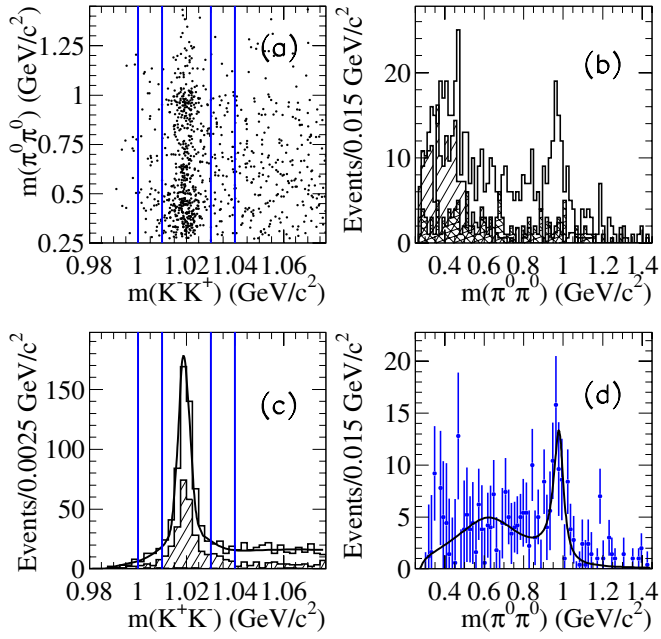

FIG. 19 (color online). (a) Scatter plot of the $\pi^0\pi^0$ invariant mass vs the K^+K^- invariant mass for all selected $K^+K^-\pi^0\pi^0$ events; (b) the $\pi^0\pi^0$ invariant-mass projections for events in the ϕ peak (open histogram), sidebands (cross-hatched) and control region (hatched); (c) the K^+K^- mass projection for events in the signal (open) and control (hatched) regions; (d) difference between the open and other histograms in (b).

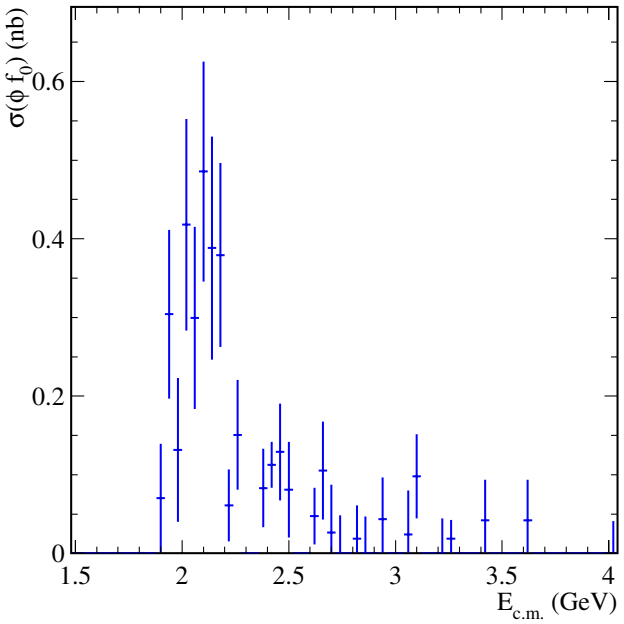

FIG. 20 (color online). Cross section for the reaction $e^+e^- \to \phi(1020)f_0(980)$ as a function of effective e^+e^- c.m. energy obtained from the $K^+K^-\pi^0\pi^0$ final state.

region histogram (hatched) in Fig. 19(c). The contributions from non-ISR and ISR $\pi^+\pi^-\pi^0\pi^0$ events are negligible. Selecting ϕ candidate and sideband events as for the $K^+K^-\pi^+\pi^-$ mode [vertical lines in Figs. 19(a) and 19(c)], we obtain the $\pi^0\pi^0$ mass projections shown as the open and cross-hatched histograms, respectively, in Fig. 19(b). Control region events (hatched histogram) are concentrated at low masses. A peak corresponding to the $f_0(980)$ is visible over a relatively low background.

In Fig. 19(d) we show the numbers of entries from the candidate events minus those from the sideband and control regions. A sum of two Breit-Wigner functions is again sufficient to describe the data. Fitting Eq. (3) with the parameters of one BW fixed to the values given in Sec. IV F, corresponding to the $f_0(600)$, we obtain a good fit, shown as the curve in Fig. 19(d). This fit yields a $f_0(980)$ signal of 54 ± 9 events with a mass $m = 0.970 \pm 0.007$ GeV/c^2 and width $\Gamma = 0.081 \pm 0.021$ GeV consistent with PDG values [5]. Because of low statistics and high backgrounds, we do not extract an $e^+e^- \to \phi(1020)\pi^0\pi^0$ cross section.

F. The $\phi(1020)f_0(980)$ intermediate state

Since the background under the $f_0(980)$ peak in Figs. 19(b) and 19(d) is relatively low, we are able to extract the $\phi(1020)f_0(980)$ contribution. As in Sec. IV G, we require the dipion mass to be in the range 0.85–1.10 GeV/c^2 and fit the background-subtracted K^+K^- mass projection in each bin of $K^+K^-\pi^0\pi^0$ mass to obtain a number of ϕf_0 events. Again, about 10% of these are $\phi\pi^0\pi^0$ events in which the $\pi^0\pi^0$ pair is not produced through the f_0, but this does not affect the conclusions.

We convert the number of fitted events in each mass bin into a measurement of the $e^+e^- \to \phi(1020)f_0(980)$ cross section as described above and divide by the $f_0(980) \to \pi^0\pi^0$ branching fraction of one-third. The cross section is shown in Fig. 20 as a function of $E_{\rm c.m.}$ and is listed in Table VIII. Due to a smaller number of events, we have used larger bins at higher energies. The overall shape is consistent with that obtained in the $K^+K^-\pi^+\pi^-$ mode (see Fig. 13), and there is a sharp drop near 2.2 GeV/c^2, but the statistical errors are large and no conclusion can be drawn from this mode alone. Possible interpretations are discussed in Sec. VII.

VI. THE $K^+K^-K^+K^-$ FINAL STATE

A. Final selection and background

Figure 21 shows the distribution of χ^2_{4K} for the $K^+K^-K^+K^-$ candidates as points, and the open histogram is the distribution for simulated $K^+K^-K^+K^-$ events, normalized to the data in the region $\chi^2_{4K} < 5$ where the backgrounds and radiative corrections are small. The hatched histogram represents the background from $e^+e^- \to q\bar{q}$ events, evaluated as for the other modes. The cross-hatched histogram represents the background from simulated ISR $K^+K^-\pi^+\pi^-$ events with both charged pions misidentified as kaons.

We define signal and control regions of $\chi^2_{4K} < 20$ and $20 < \chi^2_{4K} < 40$, respectively. The signal region contains 2305 data and 20 616 simulated events, and the control

TABLE VIII. Measurements of the $e^+e^- \to \phi(1020)f_0(980)$ cross section ($f_0 \to \pi^0\pi^0$, errors are statistical only).

$E_{\rm c.m.}$ (GeV)	σ (nb)	$E_{\rm c.m.}$ (GeV)	σ (nb)	$E_{\rm c.m.}$ (GeV)	σ (nb)
1.88–1.92	$0.078^{+0.082}_{-0.053}$	2.12–2.16	$0.397^{+0.164}_{-0.137}$	2.44–2.52	$0.120^{+0.053}_{-0.042}$
1.92–1.96	$0.220^{+0.114}_{-0.085}$	2.16–2.20	$0.408^{+0.143}_{-0.118}$	2.52–2.68	$0.050^{+0.024}_{-0.019}$
1.96–2.00	$0.136^{+0.104}_{-0.075}$	2.20–2.24	$0.070^{+0.064}_{-0.042}$	2.68–2.84	$0.026^{+0.017}_{-0.012}$
2.00–2.04	$0.446^{+0.160}_{-0.131}$	2.24–2.28	$0.174^{+0.095}_{-0.071}$	2.84–3.00	$0.026^{+0.015}_{-0.011}$
2.04–2.08	$0.315^{+0.142}_{-0.113}$	2.28–2.36	$0.069^{+0.042}_{-0.030}$	3.00–3.16	$0.032^{+0.017}_{-0.013}$
2.08–2.12	$0.519^{+0.169}_{-0.141}$	2.36–2.44	$0.112^{+0.051}_{-0.040}$	3.16–3.32	$0.012^{+0.012}_{-0.008}$

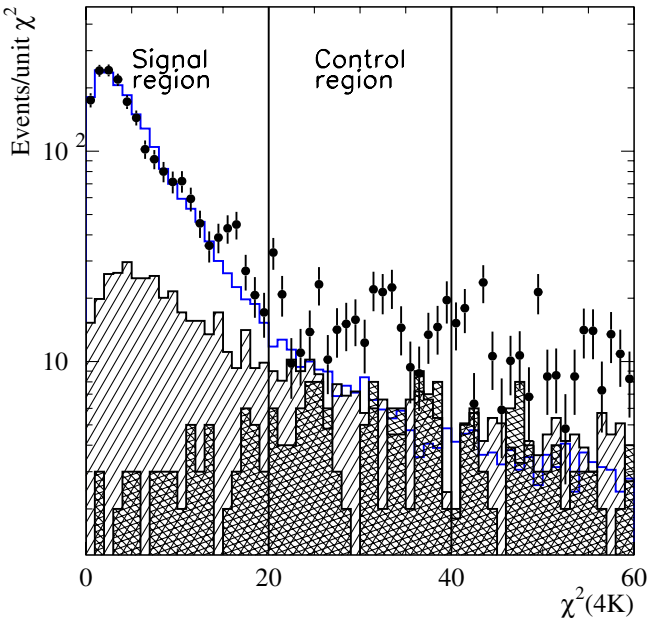

FIG. 21 (color online). Distribution of χ^2 from the three-constraint fit for $K^+K^-K^+K^-$ candidates in the data (points). The open histogram is the distribution for simulated signal events, normalized as described in the text. The hatched histogram represents the background from non-ISR events, estimated as described in the text. The cross-hatched histogram is for simulated ISR $K^+K^-\pi^+\pi^-$ events.

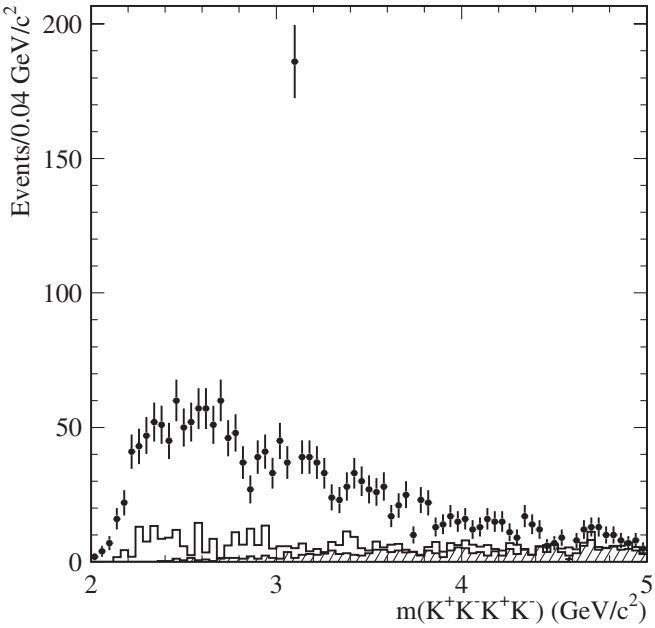

FIG. 22. Invariant-mass distribution for $K^+K^-K^+K^-$ candidates in the data (points). The hatched and open histograms represent, cumulatively, the non-ISR background and the ISR background from the control region, which is dominated by the contribution from ISR $K^+K^-\pi^+\pi^-$ events.

region contains 463 data and 1601 simulated events. Figure 22 shows the $K^+K^-K^+K^-$ invariant-mass distribution from threshold up to 5 GeV/c^2 for events in the signal region as points with errors. The $q\bar{q}$ background (hatched histogram) is small at low masses, but dominant above about 4.5 GeV/c^2. Since the ISR $K^+K^-\pi^+\pi^-$ background does not peak at low χ^2_{4K} values, we include it in the background evaluated from the control region, according to the method explained in Sec. IV A. It dominates this background, which is 10% or lower at all masses. The total background is shown as the open histogram in Fig. 22.

We subtract the sum of backgrounds from the number of selected events in each mass bin to obtain a number of signal events. Considering uncertainties in the cross sections for the background processes, the normalization of events in the control region, and the simulation statistics, we estimate a systematic uncertainty on the signal yield of less than 5% in the 2–3 GeV/c^2 region, increasing to 10% in the region above 3 GeV/c^2.

B. Selection efficiency

The detection efficiency is determined as for the other two final states. Figure 23(a) shows the simulated $K^+K^-K^+K^-$ invariant-mass distributions in the signal and control regions from the phase space model. We divide the number of reconstructed events in each mass interval by the number of generated ones in that interval to obtain the efficiency shown as the points in Fig. 23(b). It is quite uniform, and we fit a third-order polynomial, which we use to extract the cross section. A factor of 0.7 is again appli-

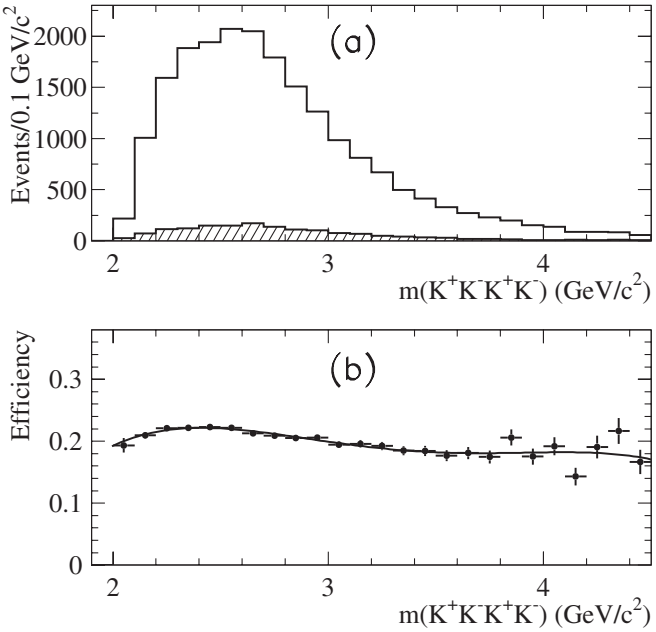

FIG. 23. (a) Invariant-mass distributions for simulated $K^+K^-K^+K^-$ events in the signal (open) and control (hatched) regions (see Fig. 21); (b) net reconstruction and selection efficiency as a function of mass obtained from this simulation (the curve represents a 3rd order polynomial fit).

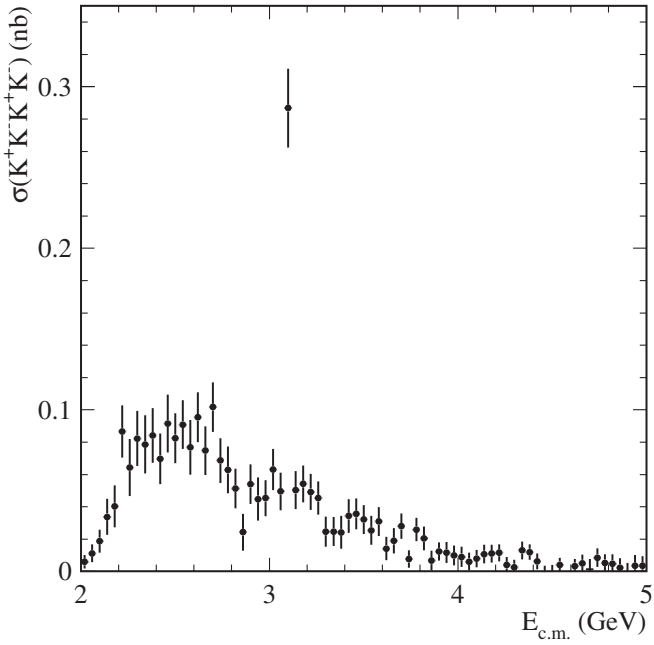

FIG. 24. The $e^+e^- \to K^+K^-K^+K^-$ cross section as a function of the effective e^+e^- c.m. energy measured with ISR data at *BABAR*. The errors are statistical only.

cable for only hadronic system efficiency due to the limited angular coverage of the ISR photon simulation. A simulation assuming dominance of the ϕK^+K^- channel, with the K^+K^- pair in an S-wave, gives consistent results, and we apply the same 5% systematic uncertainty as for the other final states. We correct for mismodeling of the track finding and kaon identification efficiencies as in Sec. IV B, and for the shape of the χ^2_{4K} distribution analogously, using the result in Ref. [11], $(3.0 \pm 2.0)\%$.

C. Cross section for $e^+e^- \to K^+K^-K^+K^-$

We calculate the $e^+e^- \to K^+K^-K^+K^-$ cross section in 40 MeV $E_{\rm c.m.}$ intervals from the analog of Eq. (2), using the invariant mass of the $K^+K^-K^+K^-$ system to determine the effective c.m. energy. We show this cross section in Fig. 24 and list it in Table IX. It rises to a peak value near 0.1 nb in the 2.3–2.7 GeV region, then decreases slowly with increasing energy. The only statistically significant narrow structure is the J/ψ peak. Again, $d\mathcal{L}$ includes corrections for vacuum polarization that should be omitted from calculations of $g_\mu - 2$. This supersedes our previous result [11].

The simulated $K^+K^-K^+K^-$ invariant-mass resolution is 3.0 MeV/c^2 in the 2.0–2.5 GeV/c^2 range, increasing with mass to 4.7 MeV/c^2 in the 2.5–3.5 GeV/c^2 range. Since the cross section has no sharp structure except for the J/ψ peak, we again make no correction for resolution. The errors shown in Fig. 24 and Table IX are statistical only. The point-to-point systematic errors are much smaller than this, and the errors on the normalization are summarized in Table X, along with the corrections applied to the measurement. The total correction is +10%, and the total systematic uncertainty is 9% at low mass, increasing to 13% above 3 GeV/c^2.

D. The $\phi(1020)K^+K^-$ intermediate state

Figure 25 shows the invariant-mass distribution for all K^+K^- pairs in the selected $K^+K^-K^+K^-$ events (4 entries per event) as the open histogram. A prominent ϕ peak is visible, along with possible peaks at 1.5, 1.7 and 2.0 GeV/c^2. The hatched histogram is for the pair in each event with mass closest to the nominal ϕ mass, and indicates that the ϕK^+K^- channel dominates the $K^+K^-K^+K^-$ final state. Our previous finding of very little

TABLE IX. Measurements of the $e^+e^- \to K^+K^-K^+K^-$ cross section (errors are statistical only).

$E_{\rm c.m.}$ (GeV)	σ (nb)	$E_{\rm c.m.}$ (GeV)	σ (nb)	$E_{\rm c.m.}$ (GeV)	σ (nb)	$E_{\rm c.m.}$ (GeV)	σ (nb)
2.02	0.006 ± 0.004	2.66	0.075 ± 0.015	3.30	0.025 ± 0.009	3.94	0.012 ± 0.006
2.06	0.011 ± 0.006	2.70	0.102 ± 0.015	3.34	0.025 ± 0.009	3.98	0.012 ± 0.006
2.10	0.019 ± 0.007	2.74	0.069 ± 0.014	3.38	0.024 ± 0.010	4.02	0.010 ± 0.006
2.14	0.034 ± 0.011	2.78	0.063 ± 0.014	3.42	0.034 ± 0.010	4.06	0.009 ± 0.005
2.18	0.040 ± 0.013	2.82	0.051 ± 0.012	3.46	0.036 ± 0.009	4.10	0.006 ± 0.005
2.22	0.087 ± 0.016	2.86	0.024 ± 0.011	3.50	0.032 ± 0.009	4.14	0.008 ± 0.006
2.26	0.064 ± 0.018	2.90	0.054 ± 0.012	3.54	0.025 ± 0.009	4.18	0.011 ± 0.005
2.30	0.082 ± 0.017	2.94	0.045 ± 0.013	3.58	0.031 ± 0.009	4.22	0.011 ± 0.005
2.34	0.079 ± 0.018	2.98	0.045 ± 0.011	3.62	0.014 ± 0.007	4.26	0.012 ± 0.005
2.38	0.084 ± 0.017	3.02	0.063 ± 0.013	3.66	0.019 ± 0.008	4.30	0.004 ± 0.005
2.42	0.070 ± 0.016	3.06	0.049 ± 0.012	3.70	0.028 ± 0.008	4.34	0.003 ± 0.006
2.46	0.092 ± 0.018	3.10	0.287 ± 0.024	3.74	0.008 ± 0.005	4.38	0.013 ± 0.005
2.50	0.082 ± 0.015	3.14	0.050 ± 0.012	3.78	0.026 ± 0.007	4.42	0.012 ± 0.005
2.54	0.091 ± 0.015	3.18	0.054 ± 0.011	3.82	0.020 ± 0.007	4.46	0.006 ± −0.004
2.58	0.077 ± 0.017	3.22	0.049 ± 0.011	3.86	0.007 ± 0.006	4.50	−0.001 ± −0.004
2.62	0.095 ± 0.015	3.26	0.045 ± 0.010	3.90	0.012 ± 0.006	4.54	0.000 ± 0.004

TABLE X. Summary of corrections and systematic uncertainties on the $e^+e^- \to K^+K^-K^+K^-$ cross section. The total correction is the linear sum of the components and the total uncertainty is the sum in quadrature.

Source	Correction	Uncertainty
Radiative corrections	...	1%
Backgrounds	...	5%, $m_{4K} < 3$ GeV/c^2
		10%, $m_{4K} > 3$ GeV/c^2
Model dependence	...	5%
χ^2_{4K} distribution	+3%	2%
Tracking efficiency	+3%	2%
Kaon ID efficiency	+4%	4%
ISR luminosity	...	3%
Total	+10%	9%, $m_{4K} < 3$ GeV/c^2
		13%, $m_{4K} > 3$ GeV/c^2

ϕ signal [11] was incorrect due to an error in the analysis algorithm.

If the pair mass closest to the ϕ mass is within 10 MeV/c^2 of the ϕ mass, then we include the invariant mass of the other K^+K^- combination in Fig. 26. The contribution from events in the J/ψ peak is shown as the hatched histogram which is in agreement with the BES experiment [23] which studied the structures around 1.5, 1.7 and 2.0 GeV/c^2 in detail. There is no evidence for the ϕf_0 channel, but there is an enhancement at threshold that can be interpreted as the tail of the $f_0(980)$. This is expected in light of the ϕf_0 cross sections measured above in

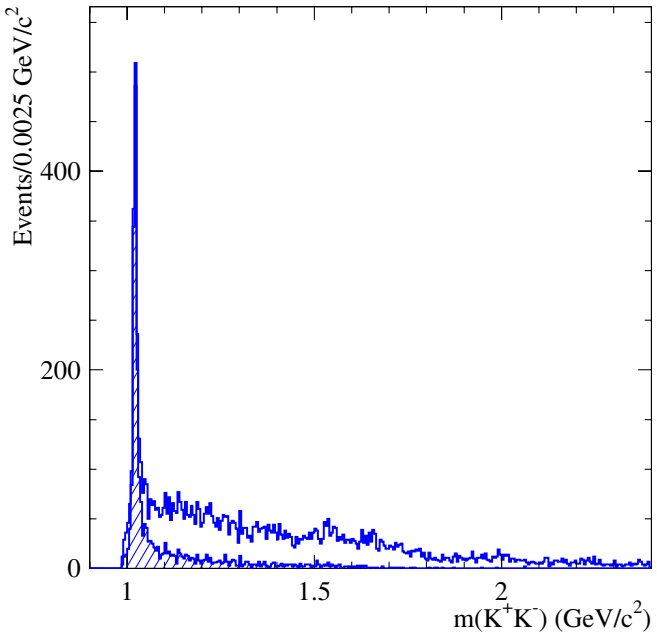

FIG. 25 (color online). Invariant-mass distributions for all K^+K^- pairs in selected $e^+e^- \to K^+K^-K^+K^-$ events (open histogram) and for the combination in each event closest to the ϕ-meson mass (hatched).

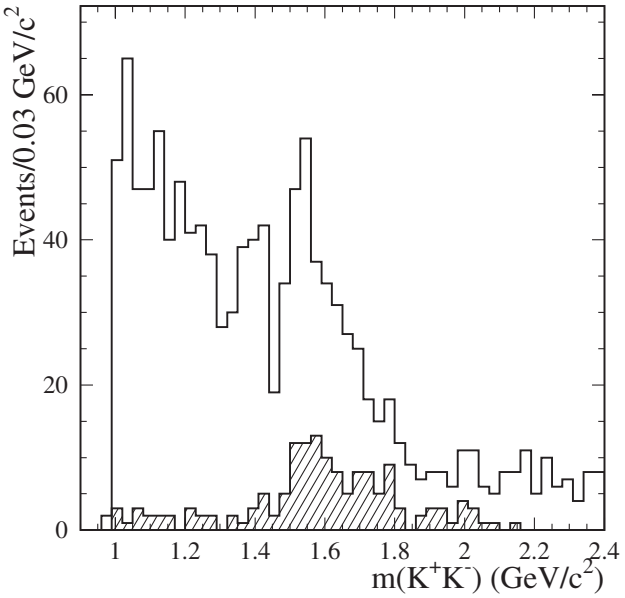

FIG. 26. Invariant-mass distribution for K^+K^- pairs in events in which the other K^+K^- pair has mass closest to and within 10 MeV/c^2 of the nominal ϕ mass (open histogram). The hatched histogram is for the subset with a $K^+K^-K^+K^-$ mass in the J/ψ peak.

the $K^+K^-\pi^+\pi^-$ and $K^+K^-\pi^0\pi^0$ final states. However, the statistics and uncertainties in the $f_0(980) \to K^+K^-$ line shape do not allow a meaningful extraction of the cross section in this final state.

We observe no significant structure in the $K^+K^-K^\pm$ mass distribution. We use these events to study the possibility that part of our $\phi\pi^+\pi^-$ signal is due to ϕK^+K^- events with the two kaons not from the ϕ taken as pions. No structure is present in the reconstructed $K^+K^-\pi^+\pi^-$ invariant-mass distribution from these events.

VII. $e^+e^- \to \phi f_0$ NEAR THRESHOLD

The behavior of the $e^+e^- \to \phi f_0$ cross section near threshold shows a structure near 2150 MeV/c^2, and we have published this result in Ref. [14]. Here we provide a more detailed study of this cross section in the 1.8–3 GeV region. In Fig. 27 we superimpose the cross sections measured in the $K^+K^-\pi^+\pi^-$ and $K^+K^-\pi^0\pi^0$ final states (shown in Figs. 13 and 20); they are consistent with each other. The $K^+K^-K^+K^-$ cross section (Sec. VI D) is also consistent with the presence of a structure near 2150 MeV/c^2 and shows a contribution from the ϕf_0 channel, but since we cannot extract a meaningful ϕf_0 cross section, we do not discuss this final state further.

First, we attempt to reproduce this spectrum with a smooth threshold function. In the absence of resonances, the only theoretical constraint on the cross section well above threshold is that it should decrease smoothly with increasing $E_{\text{c.m.}}$. However the form of the cutoff at threshold is determined by the properties of the intermediate resonances and the final-state particle spins, phase space

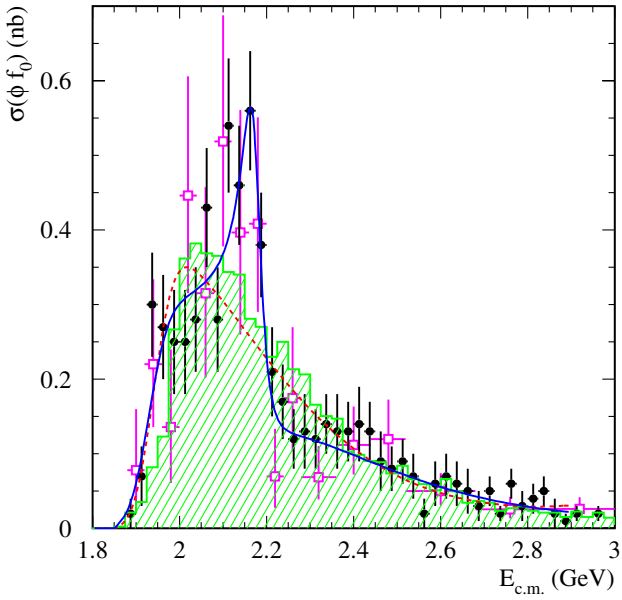

FIG. 27 (color online). The $e^+e^- \to \phi(1020)f_0(980)$ cross section measured in the $K^+K^-\pi^+\pi^-$ (circles) and $K^+K^-\pi^0\pi^0$ (squares) final states. The hatched histogram shows the simulated cross section, assuming no resonant structure. The solid (dashed) line represents the result of the one-resonance (no-resonance) fit described in the text.

and detector resolution. The model discussed in Sec. IV F takes the ϕ and $f_0(980)$ line shapes, the spins of all particles and their phase space into account, and postulates a simple $E_{\rm c.m.}^{-4}$ dependence of the cross section. For the $e^+e^- \to \phi f_0$ reaction, it predicts the cross section shown as the hatched histogram in Fig. 27, normalized to the same total area as the data. It shows a sharp rise from the threshold with a peak near 2070 MeV and is inconsistent with the data.

To account for uncertainties in the f_0 width and the shape of the cross section well above threshold, we seek a functional form that describes the simulation and whose parameters can be varied to cover a reasonable range of possibilities. This can be achieved by the product of a phase space term, an exponential rise and a second order polynomial:

$$\begin{aligned} \sigma_{nr}(\mu) &= P(\mu)\cdot A_{nr}(\mu), \\ A_{nr}(\mu) &= \sigma_0\cdot(1-e^{-(\mu/a_1)^4})\cdot(1+a_2\mu+a_3\mu^2), \\ P(\mu) &= \sqrt{1-m_0^2/(m_0+\mu)^2}, \\ \mu &= E_{\rm c.m.}-m_0, \end{aligned} \tag{4}$$

where the a_i are free parameters, σ_0 is a normalization factor, and $P(\mu)$ is a good approximation of the two-body phase space for particles with similar masses. Both the $\phi(1020)$ and $f_0(980)$ have small but finite widths, and our selection criterion of $m(\pi\pi) > 0.85$ GeV/c^2 defines an effective minimum mass, $m_0 = 1.8$ GeV/c^2. Fitting Eq. (4) to the simulated cross section yields the a_i values listed in the first column of Table XI. Fitting to the data with all a_i fixed to these values and σ_0 floating yields $\chi^2/\text{n.d.f.} = 86/(56-2)$. Floating a_2 and a_3 in addition, we obtain $\chi^2/\text{n.d.f.} = 85/(56-4)$ with a confidence level (C.L.) of 0.0025. If we float all parameters in Eq. (4), the fit yields $\chi^2/\text{n.d.f.} = 80/(56-5)$ with C.L. of 0.0053. The results of these fits are listed in Table XI, and the latter is shown as the dashed curve on Fig. 27; all fits are inconsistent with the data.

We now add a resonance and fit the data with the function

$$\begin{aligned} \sigma_{1r}(\mu) &= \frac{P(\mu)}{P(m_1)}\cdot|A_{nr}(\mu)e^{i\psi_1}+A_{r1}(\mu)|^2, \\ A_{r1}(\mu) &= \frac{\sqrt{\sigma_1}m_1\Gamma_1}{m_1^2-E_{\rm c.m.}^2-iE_{\rm c.m.}\Gamma_1}, \end{aligned} \tag{5}$$

where m_1 and Γ_1 are the mass and width of the resonance, σ_1 is its peak cross section, and ψ_1 is its phase relative to the nonresonant component. We obtain good fits both assuming no interference between the two components, $\psi_1 = \pi$, and with ψ_1 floating. The result of the latter fit is shown as the solid curve on Fig. 27. The data are somewhat above this curve near 2.4 GeV/c^2 and a fit with two resonances can also describe the data. Because of the sharp drop near 2.2 GeV/c^2, the single-resonance fit with interference gives a resonance mass about 30 MeV/c^2 higher than the other two fits. All these fits, with or without resonances, give a peak nonresonant cross section in the range 0.3–0.4 nb, which is of independent theoretical interest, because it can be related to the $\phi \to f_0(980)\gamma$ decay studied at the ϕ-factory [24].

Under the hypothesis of one resonance interfering with the nonresonant component, the fit gives the resonance parameters

$$\begin{aligned} \sigma_1 &= 0.13 \pm 0.04 \text{ nb}, \\ m_1 &= 2.175 \pm 0.010 \text{ GeV}/c^2, \\ \Gamma_1 &= 0.058 \pm 0.016 \text{ GeV}, \quad \text{and} \\ \psi_1 &= -0.57 \pm 0.30 \text{ radians}, \end{aligned}$$

along with $\chi^2/\text{n.d.f.} = 37.6/(56-9)$ (C.L. 0.84). We can

TABLE XI. Parameter values, χ^2 values and confidence levels from the fits of Eq. (4) to the data described in the text. An asterisk denotes a value that was fixed in that fit.

Fit	All a_i fixed	Only a_1 fixed	All a_i free
σ_0	1.19 ± 0.03	1.23 ± 0.03	1.09 ± 0.01
a_1	0.218^*	0.218^*	0.174 ± 0.012
a_2	-1.68^*	-1.51 ± 0.15	-1.49 ± 0.12
a_3	0.81^*	0.66 ± 0.14	0.63 ± 0.11
$\chi^2/\text{n.d.f.}$	86.4/54	85.3/52	80.5/51
$P(\chi^2)$	0.0035	0.0025	0.0053

estimate the product of its electronic width and branching fraction to ϕf_0 as

$$\mathcal{B}_{\phi f_0} \cdot \Gamma_{ee} = \frac{\Gamma_1 \sigma_1 m_1^2}{12\pi C} = (2.5 \pm 0.8 \pm 0.4)\ \text{eV},$$

where we fit the product $\Gamma_1\sigma_1$ to reduce correlations, and the conversion constant $C = 0.389$ mb$(\text{GeV}/c^2)^2$. The second error is systematic and corresponds to the normalization errors on the cross section.

The significance of the structure calculated from the change in χ^2 between the best fit and the null hypothesis is 6.2 standard deviations. Since this calculation can be unreliable in the case of low statistics and functions that vary rapidly on the scale of the bin size, we perform a set of simulations in which we generate a number of events according to a Poisson distribution about the number observed in the data and with a mass distribution given by either the simulation or fitted function in Fig. 27 without resonant structure. On each sample, we perform fits to Eqs. (4) and (5) and calculate the difference in χ^2. The fraction of trials giving a χ^2 difference larger than that seen in the data corresponds to a significance of approximately 5 standard deviations.

We search for this structure in other submodes with different and/or fewer intermediate resonances. The total cross sections are dominated by $K^*K\pi$ channels, and the $K^{*0}K^+\pi^-$ cross section is shown in Fig. 8. There is no significant structure in the 2.1–2.5 GeV region, but the point-to-point statistical uncertainties are large. If we remove events within the bands in Figs. 5 and 18, then most of the events containing a K^* are eliminated and we obtain the raw mass distributions shown as the points with errors in Figs. 28 and 29, respectively. Both distributions show evidence of a structure around 2.15 GeV$/c^2$ and the $K^+K^-\pi^+\pi^-$ distribution also shows a structure near 2.4 GeV$/c^2$. We cannot exclude the presence of these structures in events with a K^*, but we can conclude that they do not dominate those events, whereas they comprise a substantial fraction of the remaining events in that mass region.

Applying the further requirement that the dipion mass be in the range 0.85–1.10 GeV$/c^2$, we remove most of the events without an f_0, and obtain the mass distributions shown as the hatched histograms in Figs. 28 and 29. Peaks are visible at both 2.15 GeV$/c^2$ and 2.4 GeV$/c^2$ in both distributions, and they contain enough events to account for the corresponding structures in the distributions for all non-K^* events. These peaks contain at least as many events as are present in the ϕf_0 samples, but the nonresonant components are higher and there is a substantial kinematic overlap between $K^+K^-f_0$ events and $K^*K\pi$ events in this mass range.

Since this $f_0(980)$ band appears to contain a large fraction of the events within the structure, we now consider all selected events with a dipion mass inside or outside this range. Figure 31 shows the mass distribution for all selected $K^+K^-\pi^0\pi^0$ events as the open histogram, and the subsets of events with $\pi^0\pi^0$ mass inside and outside the range 0.85–1.10 GeV$/c^2$ as the hatched and cross-hatched histograms, respectively. It is evident that the $K^+K^-f_0$

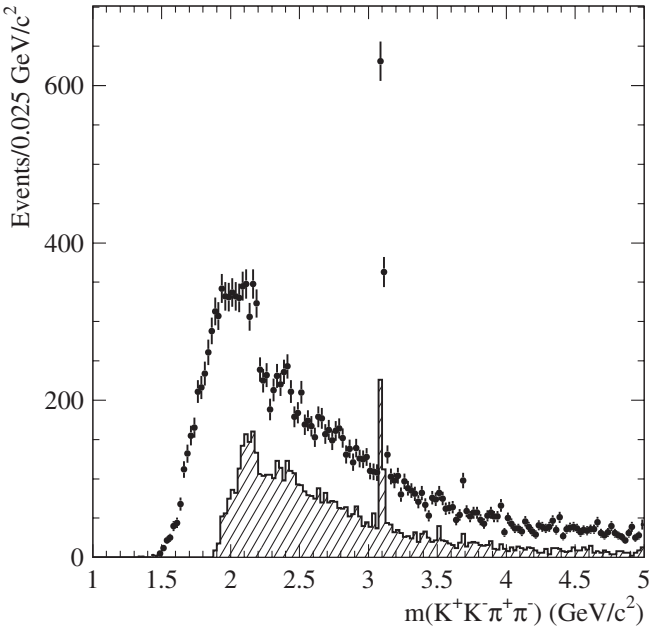

FIG. 28. Invariant-mass distribution for all selected $K^+K^-\pi^+\pi^-$ events lying outside the $K^{*0}(892)$ bands of Fig. 5 (points), and the subset of these events with $0.85 < m(\pi^+\pi^-) < 1.10$ GeV$/c^2$ (hatched).

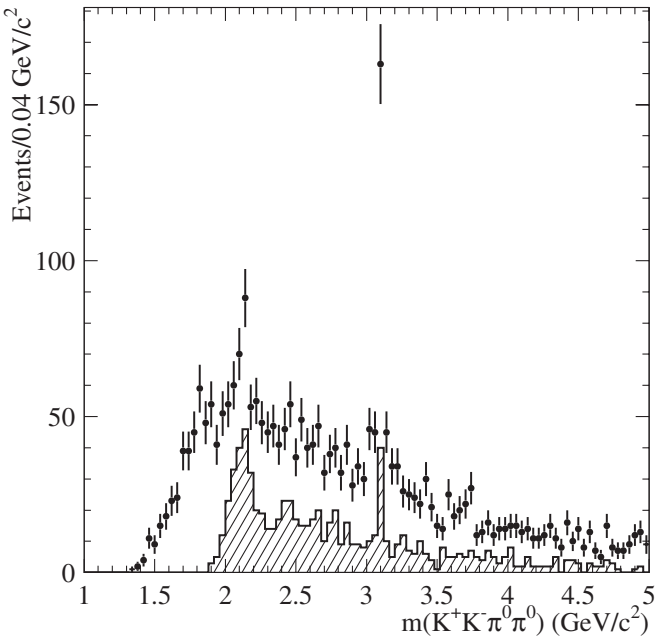

FIG. 29. Invariant-mass distribution for all selected $K^+K^-\pi^0\pi^0$ events lying outside the $K^{*0}(892)$ bands of Fig. 18 (points), and the subset of these events with $0.85 < m(\pi^0\pi^0) < 1.10$ GeV$/c^2$ (hatched).

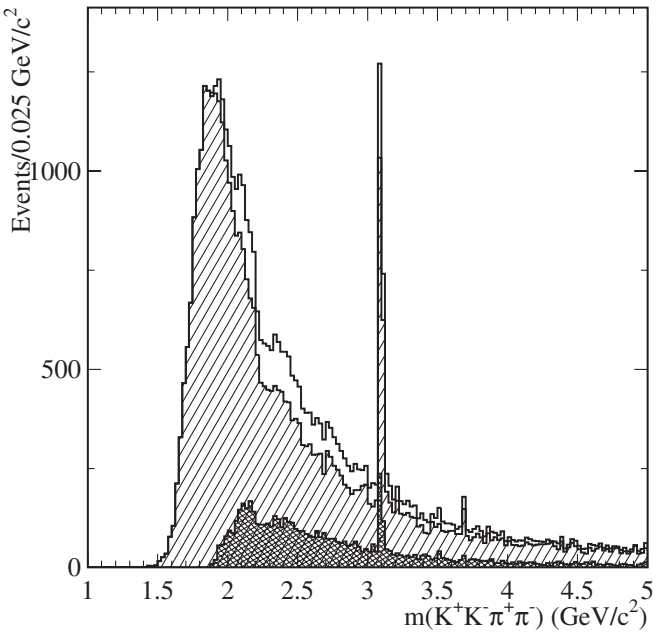

FIG. 30. The $K^+K^-\pi^+\pi^-$ invariant-mass distribution for all selected events (open histogram), and for those with a $\pi^+\pi^-$ mass inside (cross-hatched) or outside (hatched) the f_0 band as defined in the text.

channel contains the majority of the structure in the 2.0–2.6 GeV$/c^2$ range.

We show the corresponding distributions for the $K^+K^-\pi^+\pi^-$ events in Fig. 30. Because of the presence of the ρ^0, the relative f_0 contribution is much smaller in this final state, but the events in the f_0 band show clear

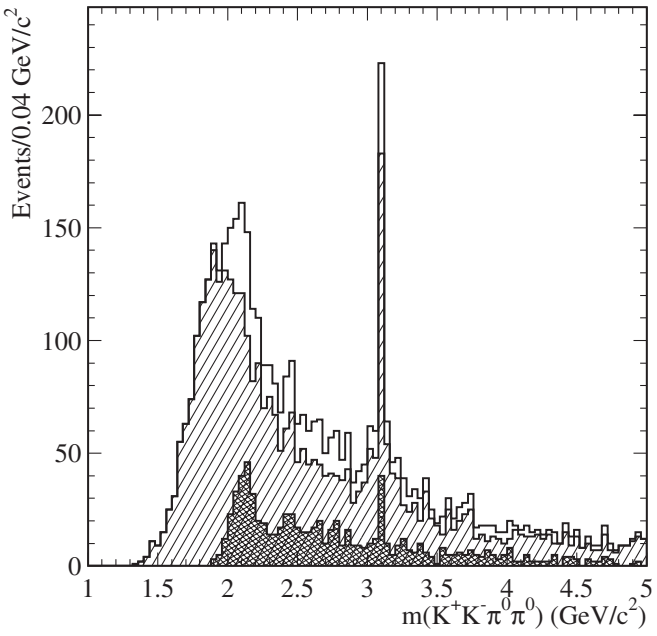

FIG. 31. The $K^+K^-\pi^0\pi^0$ invariant-mass distribution for all selected events (open histogram), and for those with a $\pi^0\pi^0$ mass inside (cross-hatched) or outside (hatched) the f_0 band as defined in the text.

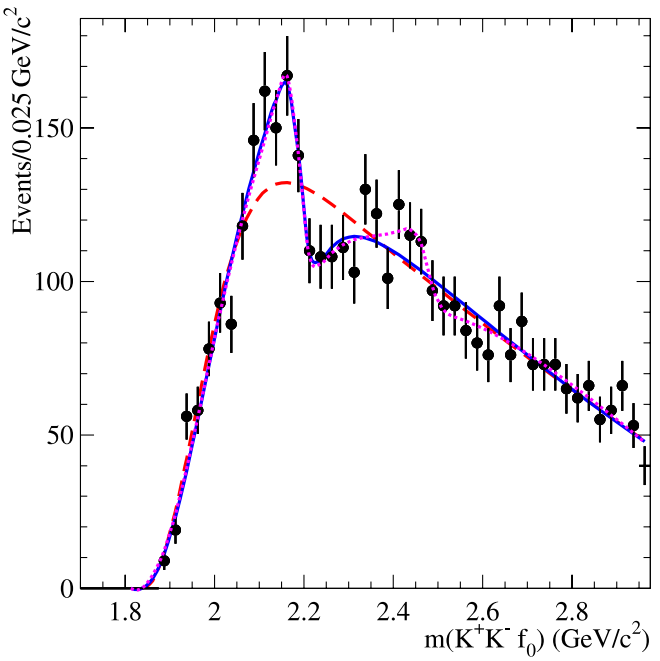

FIG. 32 (color online). The $K^+K^-\pi^+\pi^-$ invariant-mass distribution in the $K^+K^-f_0(980)$ threshold region for events with a $\pi^+\pi^-$ mass inside the f_0 band. The lines represent the results of the fits including no (dashed), one (solid) and two (dotted) resonances described in the text.

indications of structure in the 2.0–2.4 GeV$/c^2$ region. The remaining events may also have structure in this region, but

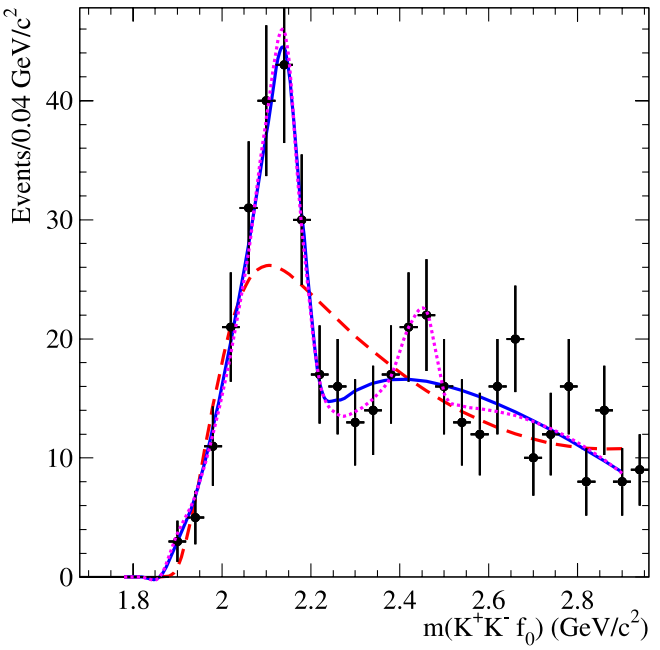

FIG. 33 (color online). The $K^+K^-\pi^0\pi^0$ invariant-mass distribution in the $K^+K^-f_0(980)$ threshold region for events with a $\pi^0\pi^0$ mass inside the f_0 band. The lines represent the results of the fits including no (dashed), one (solid) and two (dotted) resonances described in the text.

the statistical significance is marginal and it could be due to other sources, such as the $\phi f_2(1270)$ threshold at 2.3 GeV/c^2.

Figures 32 and 33 show enlarged views of the mass distributions within the f_0 bands from Figs. 30 and 31, respectively. The two-peak structure is more evident here than in the ϕf_0 events. The $0.85 < m(\pi\pi) < 1.10$ GeV/c^2 requirement gives enough phase space for K^+K^- invariant mass to cover the region from threshold to $\sim$1.3 GeV/c^2 for $m(K^+K^-\pi\pi) \approx 2.15$ GeV/c^2. From the measured kaon form factor we expect to find only about two-thirds of K^+K^- P-wave in our fitted ϕ peak. Since the non-ISR and ISR $\pi\pi\pi\pi$ backgrounds have not been subtracted and the samples contain an unknown mixture of intermediate states, we fit them with a modified version of Eq. (5) that allows up to two resonances,

$$F(\mu) = (a_4 \cdot A_{nr})^2 + |(1 - a_4)A_{nr} + A_{r1}e^{i\psi_1} + A_{r2}e^{i\psi_2}|^2. \quad (6)$$

Here, the normalization is in terms of events rather than cross section ($\sigma_i \to N_i$) and a fraction a_4 of the nonresonant component does not interfere with the resonances. We first fit the distribution with no resonances (and $a_4 = 1$). The results are shown as the dashed lines in Figs. 32 and 33 and listed in Table XII; both are inconsistent with the data.

We next include one resonance in the fit. The parameter a_4 is not well constrained by the data and its value has a small influence on all other fit parameters except for the number of events assigned to the resonance, so we present results with a_4 fixed to the reasonable values of 0.75 and 0.50 for the $K^+K^-\pi^+\pi^-$ and $K^+K^-\pi^0\pi^0$ data, respectively. The results are shown as the solid lines in Figs. 32 and 33 and listed in Table XII. The fit quality is good in both cases, the fitted resonance parameters are consistent with those from the ϕf_0 study, and the calculated significance of the structure for the $K^+K^-\pi^+\pi^-$ data is similar, 5.2 standard deviations. The $K^+K^-\pi^0\pi^0$ data show much more pronounced structure than in the ϕf_0 study, allowing a full fit to this sample with a significance of 5.0 standard deviations.

We then add a second resonance to the fit, keeping a_4 fixed and floating all other parameters. The results are shown as the dotted lines in Figs. 32 and 33, and listed in Table XII. These fits are also of good quality, but do not change the χ^2 C.L. or the parameters of the first resonance significantly. We also perform fits with no interference between the nonresonant component and any resonance ($a_4 = 1$), obtaining good quality fits for both one resonance and two resonances with relative phase $\pi/2$. The fitted resonance parameters are consistent in all cases, except that the mass of the first resonance is lower by about 50 MeV/c^2, similar to the 30 MeV/c^2 shift seen in the ϕf_0 study.

From these studies, we conclude that we have observed a new vector structure at a mass of about 2150 MeV/c^2 with a significance of over 6 standard deviations. It decays into $K^+K^-f_0(980)$, with the K^+K^- pair produced predominantly via the $\phi(1020)$. There is an additional structure at about 2400 MeV/c^2, and the two structures can be described by either two resonances or a single resonance that interferes with the nonresonant $K^+K^-f_0(980)$ process. More data and searches in other final states are needed to understand the nature of these structures.

If the main structure is due to a resonance, then it is relatively narrow and might be interpreted as the strange analog of the recently observed charmed $Y(4260)$ state [6], which decays to $J/\psi\pi^+\pi^-$. The value of $\mathcal{B}_{\phi f_0} \cdot \Gamma_{ee} = (2.5 \pm 0.8 \pm 0.4)$ eV measured here is similar to the value

TABLE XII. Summary of parameters obtained from the fits described in the text to the $K^+K^-\pi^+\pi^-$ and $K^+K^-\pi^0\pi^0$ events with dipion mass in the $f_0(980)$ band. An asterisk denotes a value that was fixed in that fit.

	No resonance		One resonance		Two resonances	
Fit	$K^+K^-\pi^+\pi^-$	$K^+K^-\pi^0\pi^0$	$K^+K^-\pi^+\pi^-$	$K^+K^-\pi^0\pi^0$	$K^+K^-\pi^+\pi^-$	$K^+K^-\pi^0\pi^0$
$N_{\rm nr}$	7204 ± 775	991 ± 202	8466 ± 334	722 ± 112	6502 ± 476	117 ± 89
a_1	0.181 ± 0.012	0.134 ± 0.017	0.224 ± 0.024	0.197 ± 0.048	0.201 ± 0.035	0.143 ± 0.053
a_2	-0.75 ± 0.21	-1.47 ± 0.38	-0.89 ± 0.17	-0.36 ± 0.10	-0.44 ± 0.15	5.80 ± 2.36
a_3	0.09 ± 0.17	0.75 ± 0.35	0.17 ± 0.08	-0.28 ± 0.14	-0.15 ± 0.12	-5.26 ± 1.75
a_4	0.75^*	0.50^*	0.75^*	0.50^*	0.75^*	0.50^*
N_1	0^*	0^*	116 ± 95	149 ± 36	163 ± 70	192 ± 44
m_1 (GeV/c^2)	$\cdots$	$\cdots$	2.192 ± 0.014	2.169 ± 0.020	2.187 ± 0.013	2.154 ± 0.029
Γ_1 (GeV)	$\cdots$	$\cdots$	0.071 ± 0.021	0.102 ± 0.027	0.066 ± 0.018	0.110 ± 0.022
ψ_1 (rad)	$\cdots$	$\cdots$	-0.60 ± 0.41	-1.02 ± 0.19	-1.10 ± 0.14	-1.04 ± 0.23
N_2	0^*	0^*	0^*	0^*	16 ± 16	6 ± 5
m_2 (GeV/c^2)	$\cdots$	$\cdots$	$\cdots$	$\cdots$	2.47 ± 0.07	2.45 ± 0.04
Γ_2 (GeV)	$\cdots$	$\cdots$	$\cdots$	$\cdots$	0.077 ± 0.065	0.062 ± 0.102
ψ_2 (rad)	$\cdots$	$\cdots$	$\cdots$	$\cdots$	0.28 ± 1.06	1.41 ± 1.29
χ^2/n.d.f.	62.8/41	38.1/21	35.6/37	13.0/17	31.4/34	9.7/13
$P(\chi^2)$	0.016	0.012	0.54	0.74	0.60	0.72

of $\mathcal{B}_{Y\to J/\psi\pi^+\pi^-}\cdot\Gamma^Y_{ee} = (5.5 \pm 1.0 \pm 0.8)$ eV reported in Ref. [6].

VIII. THE CHARMONIUM REGION

The data at masses above 3 GeV/c^2 can be used to measure or set limits for the branching fractions of narrow resonances, such as charmonia, and the narrow J/ψ and $\psi(2S)$ peaks allow measurements of our mass scale and resolution. Figures 34–36 show the invariant-mass distributions for the selected $K^+K^-\pi^+\pi^-$, $K^+K^-\pi^0\pi^0$ and $K^+K^-K^+K^-$ events, respectively, in this region, with finer binning than in the corresponding Figs. 2, 15, and 22. We do not subtract any background from the $K^+K^-\pi^+\pi^-$ or $K^+K^-K^+K^-$ data, since it is small and nearly uniformly distributed, but we use the $\chi^2_{KK\pi^0\pi^0}$ control region to subtract part of the ISR background from the $K^+K^-\pi^0\pi^0$ data. Signals from the J/ψ are visible in all three distributions, and the $\psi(2S)$ is visible in the $K^+K^-\pi^+\pi^-$ mode.

We fit each of these distributions using a sum of two Gaussian functions to describe the J/ψ and $\psi(2S)$ signals plus a polynomial to describe the remainder of the distribution. We take the signal function parameters from the simulation, but let the overall mean and width float in the fit, along with the amplitude and the coefficients of the polynomial. The fits are of good quality and are shown as the curves on Figs. 34–36. In all cases, the fitted mean value is within 1 MeV/c^2 of the PDG [5] J/ψ or $\psi(2S)$ mass, and the width is consistent within 10% with the simulated resolution discussed in Sec. IV C, V C or VI C.

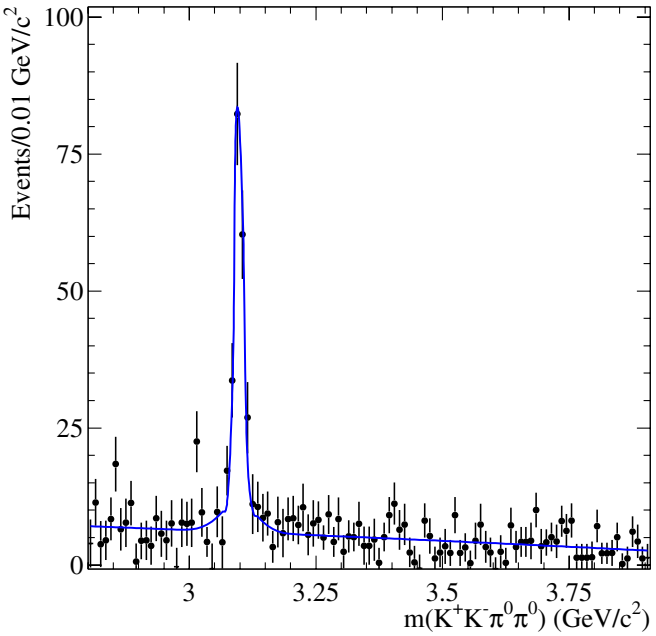

FIG. 35 (color online). Invariant-mass distribution for $e^+e^-\to K^+K^-\pi^0\pi^0$ events in the charmonium region, after partial background subtraction. The line represents the result of the fit described in the text.

The fits yield 1586 ± 58 events in the J/ψ peak for the $K^+K^-\pi^+\pi^-$ final state, 203 ± 16 events for $K^+K^-\pi^0\pi^0$ and 156 ± 15 events for $K^+K^-K^+K^-$. From these numbers of observed events in each final state f, $N_{J/\psi\to f}$, we calculate the product of the J/ψ branching fraction to f

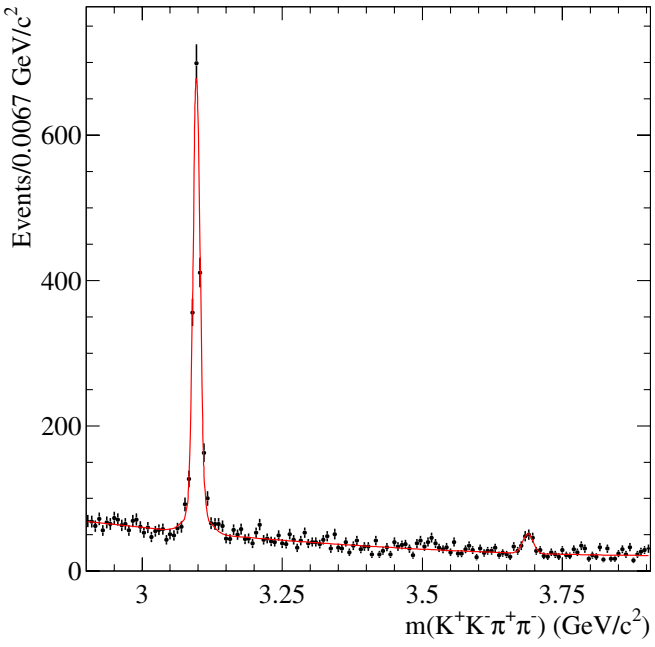

FIG. 34 (color online). Raw invariant-mass distribution for all selected $e^+e^-\to K^+K^-\pi^+\pi^-$ events in the charmonium region. The line represents the result of the fit described in the text.

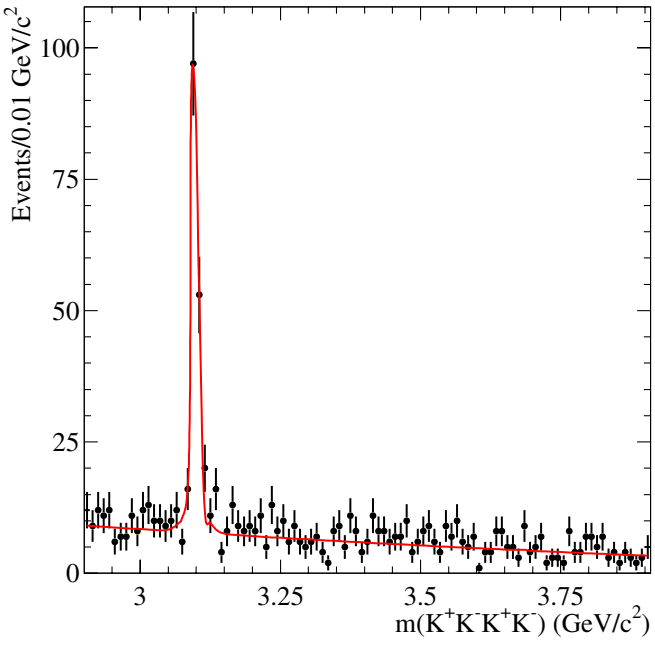

FIG. 36 (color online). Raw invariant-mass distribution for all selected $e^+e^-\to K^+K^-K^+K^-$ events in the charmonium region. The line represents the result of the fit described in the text.

and the J/ψ electronic width:

$$\mathcal{B}_{J/\psi\to f}\cdot\Gamma_{ee}^{J/\psi} = \frac{N_{J/\psi\to f}\cdot m_{J/\psi}^2}{6\pi^2\cdot d\mathcal{L}/dE\cdot\epsilon_f(m_{J/\psi})\cdot C}, \qquad (7)$$

where $d\mathcal{L}/dE = 89.8\ \mathrm{nb}^{-1}/\mathrm{MeV}$ and $\epsilon_f(m_{J/\psi})$ are the ISR luminosity and corrected selection efficiency, respectively, at the J/ψ mass and C is the conversion constant. We estimate $\epsilon_{K^+K^-\pi^+\pi^-} = 0.202$, $\epsilon_{K^+K^-\pi^0\pi^0} = 0.069$ and $\epsilon_{K^+K^-K^+K^-} = 0.176$.

Using $\Gamma_{ee}^{J/\psi} = 5.40 \pm 0.18$ keV [5], we obtain the branching fractions listed in Table XIII, along with the measured products and the current PDG values. The systematic errors include a 3% uncertainty on $\Gamma_{ee}^{J/\psi}$. The branching fractions to $K^+K^-\pi^+\pi^-$ and $K^+K^-K^+K^-$ are more precise than the current PDG values, which were dominated by our previous results of $(6.25 \pm 0.80)\times 10^{-3}$ and $(7.4 \pm 1.8)\times 10^{-4}$, respectively [11]. This is the first measurement of the $K^+K^-\pi^0\pi^0$ branching fraction.

These fits also yield 91 ± 15 $K^+K^-\pi^+\pi^-$ events in the $\psi(2S)$ peak, but no other significant signals. We expect 6.3 events from $\psi(2S)\to J/\psi\pi^+\pi^-\to K^+K^-\pi^+\pi^-$ from the relevant branching fractions [5], which is less than the statistical error. Subtracting this contribution and using a calculation analogous to Eq. (7), with $d\mathcal{L}/dE = 115.3\ \mathrm{nb}^{-1}/\mathrm{MeV}$, we obtain the product of the $\psi(2S)\to K^+K^-\pi^+\pi^-$ branching fraction and its electronic width. Dividing by the world average value of $\Gamma_{ee}^{\psi(2S)}$ [5], we obtain the branching fraction listed in Table XIII; it is consistent with the current PDG value [5].

As noted in Sec. IV D and shown in Fig. 5, the $K^+K^-\pi^+\pi^-$ final state is dominated by the $K^{*0}(892)K\pi$ channels, with a small fraction seen in the $K^{*0}(892)\bar{K}_2^{*0}(1430)$ + c.c. channels. Figure 37 shows a scatter plot of the invariant mass of a $K^\pm\pi^\mp$ pair versus that of the $K^+K^-\pi^+\pi^-$ system in events with the other

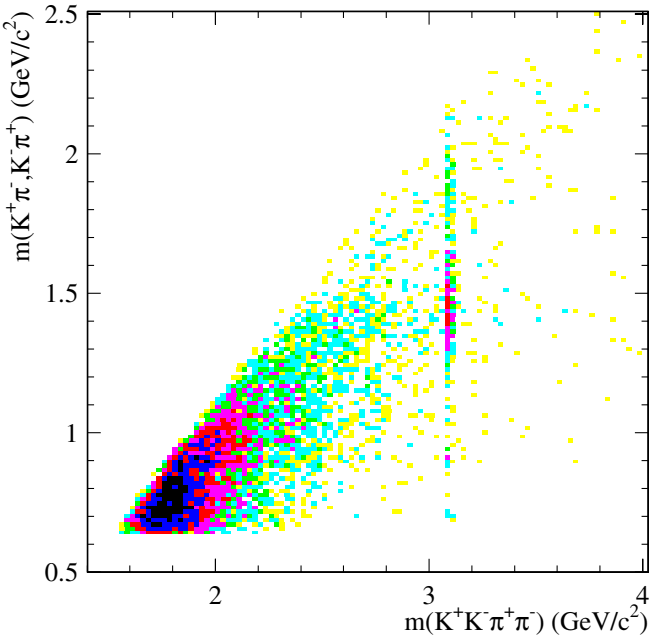

FIG. 37 (color online). The $K^\pm\pi^\mp$ invariant-mass versus $K^+K^-\pi^+\pi^-$ invariant-mass for events with the other $K^\mp\pi^\pm$ combination in the $K^{*0}(892)$ bands of Fig. 5(a). The overlapped region is taken only once.

$K^\mp\pi^\pm$ pair near the $K^{*0}(892)$ mass, i.e. within the bands in Fig. 5(a) with overlapped region taken only once. There is a large concentration of entries in the J/ψ band with $K^\pm\pi^\mp$ masses near 1430 MeV/c^2, but no solid evidence for a horizontal band corresponding to $\bar{K}_2^{*0}(1430)$ production other than in J/ψ decays. We show the $K^\pm\pi^\mp$ mass projection for the subset of events with a $K^+K^-\pi^+\pi^-$ mass within 50 MeV/c^2 of the J/ψ mass in Fig. 38 as the open histogram. The hatched histogram is the projection for events with a $K^+K^-\pi^+\pi^-$ mass between 50 and 100 MeV/c^2 below the J/ψ mass.

TABLE XIII. Summary of the J/ψ and $\psi(2S)$ branching fractions measured in this article.

Measured quantity	Measured value (eV)	J/ψ or $\psi(2S)$ branching fraction (10^{-3}) Calculated, this work	PDG2006
$\Gamma_{ee}^{J/\psi}\cdot\mathcal{B}_{J/\psi\to K^+K^-\pi^+\pi^-}$	$36.3 \pm 1.3 \pm 2.1$	$6.72 \pm 0.24 \pm 0.40$	6.2 ± 0.7
$\Gamma_{ee}^{J/\psi}\cdot\mathcal{B}_{J/\psi\to K^+K^-\pi^0\pi^0}$	$13.6 \pm 1.1 \pm 1.3$	$2.52 \pm 0.20 \pm 0.25$	No entry
$\Gamma_{ee}^{J/\psi}\cdot\mathcal{B}_{J/\psi\to K^+K^-K^+K^-}$	$4.11 \pm 0.39 \pm 0.30$	$0.76 \pm 0.07 \pm 0.06$	0.78 ± 0.14
$\Gamma_{ee}^{J/\psi}\cdot\mathcal{B}_{J/\psi\to K^{*0}\bar{K}_2^{*0}}\cdot\mathcal{B}_{K^{*0}\to K\pi}\cdot\mathcal{B}_{K_2^{*0}\to K\pi}$	$7.3 \pm 0.5 \pm 0.6$	$2.7 \pm 0.2 \pm 0.2$	6.7 ± 2.6
$\Gamma_{ee}^{J/\psi}\cdot\mathcal{B}_{J/\psi\to K^{*0}\bar{K}^{*0}}\cdot\mathcal{B}_{K^{*0}\to K\pi}\cdot\mathcal{B}_{\bar{K}^{*0}\to K\pi}$	$0.57 \pm 0.18 \pm 0.05$	$0.11 \pm 0.04 \pm 0.01$	<0.5 at 90% C.L.
$\Gamma_{ee}^{J/\psi}\cdot B_{J/\psi\to K^{*0}K_2(1770)}\cdot\mathcal{B}_{K^{*0}\to K\pi}\cdot\mathcal{B}_{K_2\to K\pi}$	$2.5 \pm 0.3 \pm 0.2$	$\cdots$	No entry
$\Gamma_{ee}^{J/\psi}\cdot\mathcal{B}_{J/\psi\to\phi\pi^+\pi^-}\cdot\mathcal{B}_{\phi\to K^+K^-}$	$2.61 \pm 0.30 \pm 0.18$	$0.98 \pm 0.11 \pm 0.07$	0.94 ± 0.15
$\Gamma_{ee}^{J/\psi}\cdot\mathcal{B}_{J/\psi\to\phi\pi^0\pi^0}\cdot\mathcal{B}_{\phi\to K^+K^-}$	$1.54 \pm 0.40 \pm 0.16$	$0.58 \pm 0.15 \pm 0.06$	No entry
$\Gamma_{ee}^{J/\psi}\cdot\mathcal{B}_{J/\psi\to\phi f_0}\cdot\mathcal{B}_{\phi\to K^+K^-}\cdot\mathcal{B}_{f_0\to\pi^+\pi^-}$	$0.50 \pm 0.11 \pm 0.04$	$0.28 \pm 0.07 \pm 0.02$	0.32 ± 0.09 ($s = 1.9$)
$\Gamma_{ee}^{J/\psi}\cdot\mathcal{B}_{J/\psi\to\phi f_0}\cdot\mathcal{B}_{\phi\to K^+K^-}\cdot\mathcal{B}_{f_0\to\pi^0\pi^0}$	$0.47 \pm 0.19 \pm 0.05$	$0.54 \pm 0.21 \pm 0.05$	0.32 ± 0.09 ($s = 1.9$)
$\Gamma_{ee}^{J/\psi}\cdot\mathcal{B}_{J/\psi\to\phi f_2}\cdot\mathcal{B}_{\phi\to K^+K^-}\cdot\mathcal{B}_{f_2\to\pi^+\pi^-}$	$1.12 \pm 0.18 \pm 0.09$	$0.50 \pm 0.08 \pm 0.04$	<0.37 at 90% C.L.
$\Gamma_{ee}^{\psi(2S)}\cdot\mathcal{B}_{\psi(2S)\to K^+K^-\pi^+\pi^-}$	$2.56 \pm 0.42 \pm 0.16$	$1.2 \pm 0.2 \pm 0.08$	0.72 ± 0.05
$\Gamma_{ee}^{\psi(2S)}\cdot\mathcal{B}_{\psi(2S)\to\phi\pi^+\pi^-}\cdot\mathcal{B}_{\phi\to K^+K^-}$	$0.28 \pm 0.11 \pm 0.02$	$0.27 \pm 0.11 \pm 0.02$	0.113 ± 0.029
$\Gamma_{ee}^{\psi(2S)}\cdot\mathcal{B}_{\psi(2S)\to\phi f_0}\cdot\mathcal{B}_{\phi\to K^+K^-}\cdot\mathcal{B}_{f_0\to\pi^+\pi^-}$	$0.17 \pm 0.08 \pm 0.02$	$0.26 \pm 0.12 \pm 0.03$	0.090 ± 0.033

The J/ψ component appears to be dominated by the $K_2^{*0}(1430)$. Also seen is a small signal from $K^{*0}(892)$ indicating the $K^{*0}(892)\bar{K}^{*0}(892)$ decay of J/ψ: this is also seen as an enhancement in the vertical J/ψ band in Fig. 37. The enhancement at 1.8 GeV/c^2 of Fig. 38 can be explained by the J/ψ decay into $K^{*0}(892)K_2(1770)$ + c.c. [or $K^{*0}(892)K_2(1820)$ + c.c.], a mode which has not previously been reported. Subtracting the number of sideband events from the number in the J/ψ mass window, we obtain 317 ± 23 events with a $K^{\pm}\pi^{\mp}$ mass in the range 1200–1700 MeV/c^2, which we take as a measure of J/ψ decays into $K^{*0}(892)\bar{K}_2^{*0}(1430)$, 25 ± 8 events in the 0.8–1.0 GeV/c^2 window for the $K^{*0}(892)\bar{K}^{*0}(892)$ decay and 110 ± 14 events for the $K^{*0}(892)K_2(1770)$ or $K^{*0}(892)K_2(1830)$ final state in the 1.7–2.0 GeV/c^2 region. We convert these to branching fractions using Eq. (7) and dividing by the known branching fractions of excited kaons [5]. The results are listed in Table XIII: they are considerably more precise than the PDG values. We cannot calculate $B_{J/\psi\to K^{*0}K_2(1770)}$ because no branching fractions of $K_2(1770)$ or $K_2(1830)$ to $K\pi$ are reported.

We study decays into $\phi\pi^+\pi^-$ and $\phi\pi^0\pi^0$ using the mass distributions shown in Figs. 39 and 40, respectively. The open histograms are for the events with a K^+K^- mass within the ϕ bands of Figs. 9(c) and 19(c). The cross-hatched histogram in Fig. 39 is from the ϕ sidebands of Fig. 9(c) and represents the dominant background in the $\phi\pi^+\pi^-$ mode. The hatched histogram in Fig. 40 is from the $\chi^2_{KK\pi^0\pi^0}$ control region and represents the dominant background in the $\phi\pi^0\pi^0$ mode. Subtracting these backgrounds, we find 103 ± 12 $J/\psi \to \phi\pi^+\pi^-$ events, 23 ± 6 $J/\psi \to \phi\pi^0\pi^0$ events, and 10 ± 4 $\psi(2S) \to \phi\pi^+\pi^-$ events. We convert these to branching fractions and list them in Table XIII. This is the first measurement of the

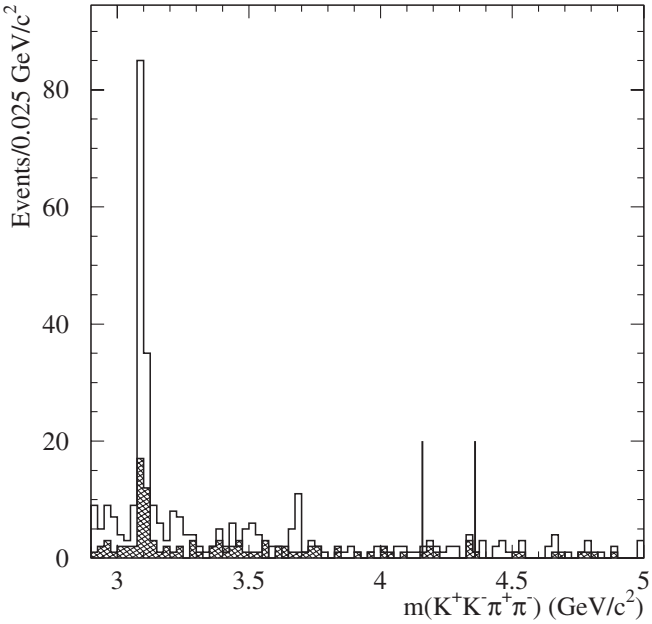

FIG. 39. Raw invariant-mass distributions for candidate $e^+e^- \to \phi\pi^+\pi^-$ events (open histogram) and events in the ϕ sidebands of Fig. 9(c) (cross-hatched) in the charmonium region. The vertical lines indicate the region used for the $Y(4260)$ search.

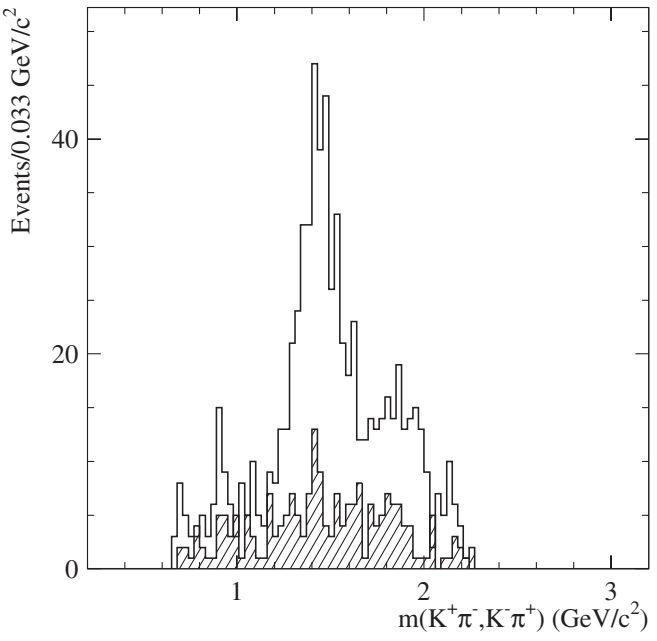

FIG. 38. The $K^{\pm}\pi^{\mp}$ mass projection from Fig. 37 for events with a $K^+K^-\pi^+\pi^-$ mass within 50 MeV/c^2 of the J/ψ mass (open histogram) and 50–100 MeV/c^2 below (hatched).

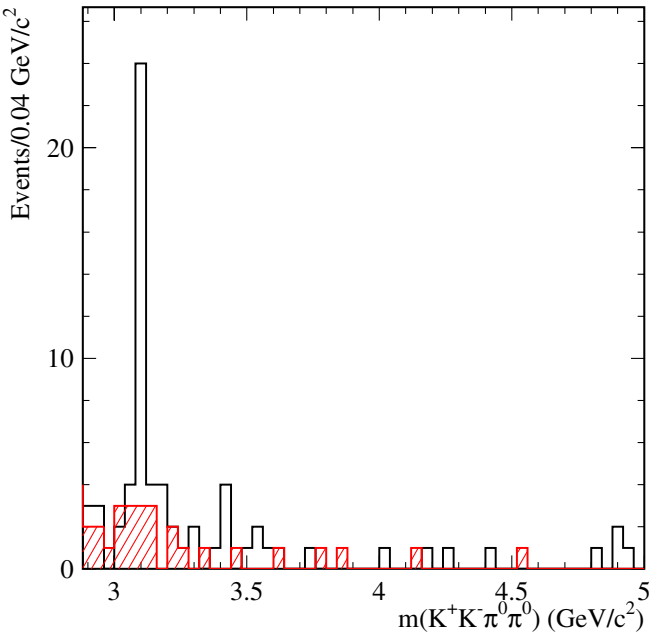

FIG. 40 (color online). Raw invariant-mass distributions for candidate $e^+e^- \to \phi\pi^0\pi^0$ events (open histogram) and events in the $\chi^2_{KK\pi^0\pi^0}$ control region (hatched) in the charmonium region.

$J/\psi \to \phi\pi^0\pi^0$ branching fraction, and the other two are consistent with current PDG values.

If the $Y(4260)$ has a substantial branching fraction into $\phi\pi^+\pi^-$, then we would expect to see a signal in Fig. 39. In the mass range $|m(\phi\pi^+\pi^-) - m(Y)| < 0.1$ GeV/c^2, we find 10 events, and assuming a uniform distribution we estimate 9.2 background events from the 3.8–5.0 GeV/c^2 region. This corresponds to a signal of 0.8 ± 3.3 events or a limit of <5 events at the 90% C.L. Using $d\mathcal{L}/dE = 147.7$ nb^{-1}/MeV at the $Y(4260)$ mass, we calculate $\mathcal{B}_{Y\to\phi\pi^+\pi^-} \cdot \Gamma^Y_{ee} < 0.4$ eV which is well below the value of $\mathcal{B}_{Y\to J/\psi\pi^+\pi^-} \cdot \Gamma^Y_{ee} = (5.5 \pm 1.0 \pm 0.8)$ eV [6]. No $Y(4260)$ signal is seen in any other mode studied here.

Figures 41(a) and 42 show the corresponding mass distributions for ϕf_0 events, i.e. the subsets of the events in Figs. 39 and 40 with a dipion mass in the range 0.85–1.10 GeV/c^2. Signals at the J/ψ mass are visible in both cases, but ϕf_0 is not the dominant mode of the $J/\psi \to \phi\pi^+\pi^-$ decay. Figure 41(b) shows the $\pi^+\pi^-$ invariant-mass distribution for events in the J/ψ peak of Fig. 39, $3.05 < m(K^+K^-\pi^+\pi^-) < 3.15$ GeV/c^2. A two-peak structure is visible that can interpreted as due to the $f_0(980)$ and $f_2(1270)$ resonances. Fitting the distribution in Fig. 41(b) with a sum of two Breit-Wigner functions with parameters fixed to PDG values [5], we find 19.5 ± 4.5 $J/\psi \to \phi f_0$ events and 44 ± 7 $J/\psi \to \phi f_2$ events. From Fig. 42 we estimate 7.0 ± 2.8 ϕf_0 events in the $\pi^0\pi^0$ mode.

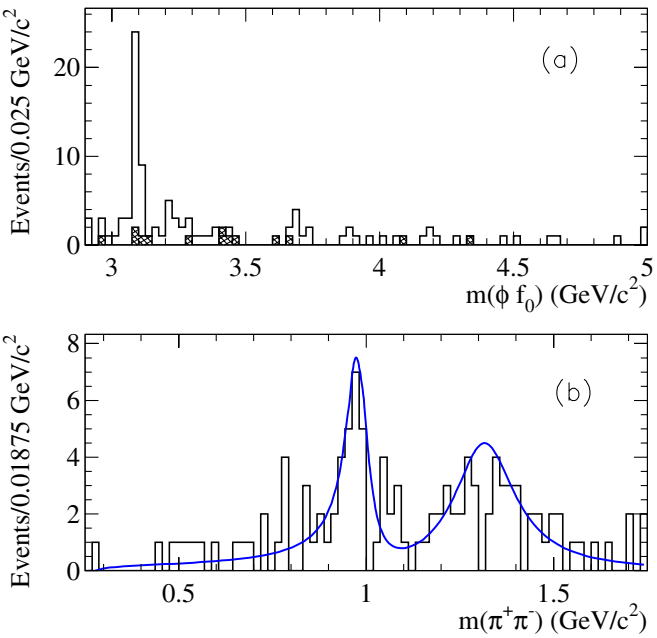

FIG. 41 (color online). (a) Raw invariant-mass distribution for candidate ϕf_0, $f_0 \to \pi^+\pi^-$ events (open histogram) and events in the ϕ sidebands (cross-hatched) in the charmonium region; (b) the $\pi^+\pi^-$ invariant-mass distribution for $\phi\pi^+\pi^-$ events from the J/ψ peak of Fig. 39. The line represents the result of the fit described in the text.

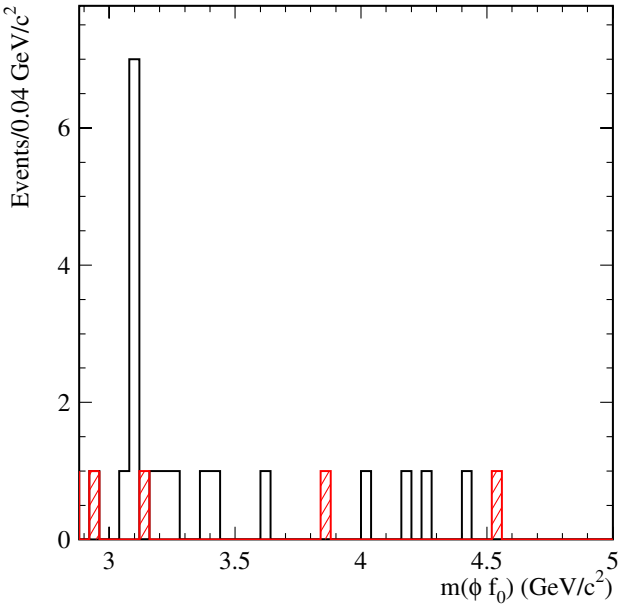

FIG. 42 (color online). Raw invariant-mass distribution for candidate ϕf_0, $f_0 \to \pi^0\pi^0$ events (open histogram) and events in the $\chi^2_{KK\pi^0\pi^0}$ control region (hatched) in the charmonium region.

Using Eq. (7) and dividing by the appropriate branching fractions, we obtain the J/ψ branching fractions listed in Table XIII. The measurements of $\mathcal{B}_{J/\psi\to\phi f_0}$ in the $\pi^+\pi^-$ and $\pi^0\pi^0$ decay modes of the f_0 are consistent with each other and with the PDG value, and combined they have roughly the same precision as listed in the PDG [5]. This is the first measurement of $\mathcal{B}_{J/\psi\to\phi f_2}$, and the value is consistent with the previous upper limit [5]. We also observe 6 ± 3 $\psi(2S) \to \phi f_0$, $f_0 \to \pi^+\pi^-$ events, which we convert to the branching fraction listed in Table XIII; it is consistent with the PDG value [5], assuming $\mathcal{B}_{f_0\to\pi^+\pi^-} = 2/3$.

In the $Y(4260)$ region we have 4 events with an estimated background of about 1 event. This corresponds to 3 ± 2 events, or a 90% C.L. upper limit of 5.6 events. We convert this to the limits

$$\mathcal{B}_{Y\to\phi f_0} \cdot \Gamma^Y_{ee} \cdot \mathcal{B}_{\phi\to K^+K^-} \cdot \mathcal{B}_{f_0\to\pi^+\pi^-} < 0.14\,\text{eV},$$
$$\mathcal{B}_{Y\to\phi f_0} \cdot \Gamma^Y_{ee} < 0.43\,\text{eV}, \quad 90\%\text{C.L.},$$

which is again much lower than the corresponding quantity for the $Y(4260) \to J/\psi\pi^+\pi^-$ decay.

IX. SUMMARY

We use the excellent charged-particle tracking and identification, and photon detection of the *BABAR* detector to fully reconstruct events of the type $e^+e^- \to \gamma e^+e^- \to \gamma K^+K^-\pi^+\pi^-$, $\gamma K^+K^-\pi^0\pi^0$ and $\gamma K^+K^-K^+K^-$, where the γ is radiated from the initial state e^+ or e^-. Such events are equivalent to direct e^+e^- annihilation at an effective c.m. energy corresponding to the mass of the hadronic

system, and we study the annihilation into these three final states at low $E_{\rm c.m.}$, from their respective production thresholds up to 5 GeV. The $K^+K^-\pi^+\pi^-$ and $K^+K^-K^+K^-$ measurements are consistent with, and supersede, our previous results [11]. This is the first measurement of the $K^+K^-\pi^0\pi^0$ final state, although some of the results were also presented in Ref. [14].

The systematic uncertainties on the normalization of the $e^+e^- \to K^+K^-\pi^+\pi^-$, $K^+K^-\pi^0\pi^0$ and $K^+K^-K^+K^-$ cross sections are 8%, 10% and 9%, respectively, for $E_{\rm c.m.} < 3$ GeV, and 10%, 14% and 13% in the 3–5 GeV range. The obtained cross sections are considerably more precise than previous measurements and cover this low-energy range completely, so they provide important input to calculations of the hadronic corrections to the anomalous magnetic moment of the muon and the fine structure constant at the Z^0 mass.

These final states exhibit complex resonant substructure. In the $K^+K^-\pi^+\pi^-$ mode we measure the cross sections for the first time for the specific channels $e^+e^- \to K^{*0}(890)K^-\pi^+$, $\phi\pi^+\pi^-$ and ϕf_0. We also observe signals for the $\rho^0(770)$, $K_1(1270)$, $K_1(1400)$, $K_2^{*0}(1430)$ and $f_2^{*0}(1270)$ resonances. It is difficult to disentangle these contributions to the final state, and we make no attempt to do so in this paper. We note that the ρ^0 signal is consistent with being due entirely to K_1 decays, and the total cross section is dominated by the $K^{*0}(892)K^-\pi^+ +$ c.c. channels, but there is no significant signal for $e^+e^- \to K^{*0}(892)\bar{K}^{*0}(892)$.

In the $K^+K^-\pi^0\pi^0$ mode we measure cross sections for $e^+e^- \to \phi f_0$ and observe signals for the $K^{*\pm}(892)$ and $K_2^{*\pm}(1430)$ resonances. Again, the total cross section is dominated by the $K^{*\pm}(892)K^{\mp}\pi^0$ channels, and there is no signal for $e^+e^- \to K^{*+}(892)K^{*-}(892)$. The $K^+K^-\pi^0\pi^0$ final state is not accessible to intermediate states containing K_1 resonances, and we note that the cross section is roughly a factor of 4 smaller over most of the range than the $K^+K^-\pi^+\pi^-$ cross section, consistent with $K^*K\pi$ dominance with a factor of 2 isospin suppression of the $\pi^0\pi^0$ final state and another factor of 2 for the relative branching fractions of the neutral and charged K^* to charged kaons.

In the $K^+K^-K^+K^-$ mode we find $e^+e^- \to \phi K^+K^-$ to be the dominant channel. With the current data sample we can say little about the other K^+K^- combination, except that there is an enhancement near threshold, consistent with the ϕf_0 channel, and that in J/ψ decays there is structure in the 1.5–2.0 GeV region, consistent with that observed by BES [23].

The ϕf_0 cross section measured in the $K^+K^-\pi^+\pi^-$ final state shows structure around 2.15 GeV and possibly 2.4 GeV, and the corresponding measurement in the $K^+K^-\pi^0\pi^0$ final state is consistent, as reported in Ref. [14]. Further investigation here reveals consistent results in the $K^+K^-K^+K^-$ final state and clear signals in the $K^+K^-f_0$ channels, with $f_0 \to \pi^+\pi^-$ and $\pi^0\pi^0$. The signals are predominantly from ϕf_0, but the relaxation of the K^+K^- mass requirement reveals a strong signal in the $K^+K^-\pi^0\pi^0$ final state. This structure can be interpreted as a strange partner (with c-quarks replaced by s-quarks) of the recently observed $Y(4260)$, which has the analogous decay mode $J/\psi\pi^+\pi^-$, or as an $s\bar{s}s\bar{s}$ state that decays predominantly to ϕf_0.

We also study charmonium decays into these final states and their intermediate channels. All nine of the J/ψ branching fractions and one of the three $\psi(2S)$ branching fractions listed in Table XIII are as precise or more precise than the current world averages. We do not observe the $Y(4260)$ in any decay mode. In particular, we find that the branching fraction for the $Y(4260) \to \phi\pi^+\pi^-$ decay, that a glueball model [8] predicts, is less than one-tenth of that to $J/\psi\pi^+\pi^-$.

ACKNOWLEDGMENTS

We are grateful for the extraordinary contributions of our PEP-II colleagues in achieving the excellent luminosity and machine conditions that have made this work possible. The success of this project also relies critically on the expertise and dedication of the computing organizations that support *BABAR*. The collaborating institutions wish to thank SLAC for its support and the kind hospitality extended to them. This work is supported by the U.S. Department of Energy and National Science Foundation, the Natural Sciences and Engineering Research Council (Canada), the Commissariat à l'Energie Atomique and Institut National de Physique Nucléaire et de Physique des Particules (France), the Bundesministerium für Bildung und Forschung and Deutsche Forschungsgemeinschaft (Germany), the Istituto Nazionale di Fisica Nucleare (Italy), the Foundation for Fundamental Research on Matter (The Netherlands), the Research Council of Norway, the Ministry of Science and Technology of the Russian Federation, Ministerio de Educación y Ciencia (Spain), and the Particle Physics and Astronomy Research Council (United Kingdom). Individuals have received support from the Marie-Curie IEF program (European Union) and the A. P. Sloan Foundation.

[1] V. N. Baier and V. S. Fadin, Phys. Lett. **27B**, 223 (1968).

[2] A. B. Arbuzov *et al.*, J. High Energy Phys. 12 (1998) 009.

[3] S. Binner, J. H. Kühn, and K. Melnikov, Phys. Lett. B **459**, 279 (1999).
[4] M. Benayoun *et al.*, Mod. Phys. Lett. A **14**, 2605 (1999).
[5] W.-M. Yao *et al.* (Review of Particle Physics), J. Phys. G **33**, 1 (2006).
[6] B. Aubert *et al.* (*BABAR* Collaboration), Phys. Rev. Lett. **95**, 142001 (2005).
[7] M. Davier, S. Eidelman, A. Hocker, and Z. Zhang, Eur. Phys. J. C **31**, 503 (2003).
[8] Shi-Lin Zhu, Phys. Lett. B **625**, 212 (2005).
[9] B. Aubert *et al.* (*BABAR* Collaboration), Phys. Rev. D **69**, 011103 (2004).
[10] B. Aubert *et al.* (*BABAR* Collaboration), Phys. Rev. D **70**, 072004 (2004).
[11] B. Aubert *et al.* (*BABAR* Collaboration), Phys. Rev. D **71**, 052001 (2005).
[12] B. Aubert *et al.* (*BABAR* Collaboration), Phys. Rev. D **73**, 052003 (2006).
[13] Cordier *et al.* (DM-1 Collaboration), Phys. Lett. **110B**, 335 (1982).
[14] B. Aubert *et al.* (*BABAR* Collaboration), Phys. Rev. D **74**, 091103(R) (2006).
[15] B. Aubert *et al.* (*BABAR* Collaboration), Nucl. Instrum. Methods Phys. Res., Sect. A **479**, 1 (2002).
[16] H. Czyż and J. H. Kühn, Eur. Phys. J. C **18**, 497 (2001).
[17] A. B. Arbuzov *et al.*, J. High Energy Phys. 10 (1997) 001.
[18] M. Caffo, H. Czyz, and E. Remiddi, Nuovo Cimento A **110**, 515 (1997); Phys. Lett. B **327**, 369 (1994).
[19] E. Barberio, B. van Eijk, and Z. Was, Comput. Phys. Commun. **66**, 115 (1991).
[20] S. Agostinelli *et al.* (GEANT4 Collaboration), Nucl. Instrum. Methods Phys. Res., Sect. A **506**, 250 (2003).
[21] T. Sjostrand, Comput. Phys. Commun. **82**, 74 (1994).
[22] S. Jadach and Z. Was, Comput. Phys. Commun. **85**, 453 (1995).
[23] M. Ablikim *et al.* (BES Collaboration), Phys. Lett. B **607**, 243 (2005).
[24] A. Aloisio *et al.* (KLOE Collaboration), Phys. Lett. B **537**, 21 (2002).